creative commons
COMMONS DEED

저작자표시-비영리-동일조건변경허락 2.0 대한민국

이용자는 아래의 조건을 따르는 경우에 한하여 자유롭게

- 이 저작물을 복제, 배포, 전송, 전시, 공연 및 방송할 수 있습니다.
- 이차적 저작물을 작성할 수 있습니다.

다음과 같은 조건을 따라야 합니다:

저작자표시. 귀하는 원저작자를 표시하여야 합니다.

비영리. 귀하는 이 저작물을 영리 목적으로 이용할 수 없습니다.

동일조건변경허락. 귀하가 이 저작물을 개작, 변형 또는 가공했을 경우에는, 이 저작물과 동일한 이용허락조건하에서만 배포할 수 있습니다.

- 귀하는, 이 저작물의 재이용이나 배포의 경우, 이 저작물에 적용된 이용허락조건을 명확하게 나타내어야 합니다.
- 저작권자로부터 별도의 허가를 받으면 이러한 조건들은 적용되지 않습니다.

저작권법에 따른 이용자의 권리는 위의 내용에 의하여 영향을 받지 않습니다.

이것은 이용허락규약(Legal Code)을 이해하기 쉽게 요약한 것입니다.

Disclaimer

dCollection

이학박사 학위논문

Universality between Domain-Wall Motions Driven by Two Distinct Forces : Magnetic Field and Electric Current

자구벽 이동의 보편성을 결정하는 두 가지 구동력 : 자기장과 전류

2012년 8월

서울대학교 대학원

물리천문학부

문 경 웅

Universality between Domain-Wall Motions Driven by Two Distinct Forces : Magnetic Field and Electric Current

Kyoung-Woong Moon

Supervised by
Professor Sug-Bong Choe

A Dissertation in Physics

Submitted to the Faculties of
Seoul National University
in Partial Fulfillment of the Requirements for the Degree of
Doctor of Philosophy

August 2012

Department of Physics and Astronomy
The Graduate College of Natural Sciences
Seoul National University

Abstract

Despite of so many diversities of natural phenomena, they are classified by a few universality classes because the phenomena have something in common. These common is stemmed from that the almost natural phenomena occurs on interfaces and the interface properties determine the natural phenomenon. Among the interface properties, the shape of the interface is the static property and depends on the symmetry and dimension of the system. Another property of interface is dynamic property that is a speed. The speed depends on driving force and the speed exhibits characteristic force-speed relation determines the universality class of the interface. Thus so many researches concentrated on the intensity of the driving force from old times.

Here, we researched a new possibility which determines the universality class of the interface. That is kinds of driving force. In nature, there are many driving forces and the forces exert a force to same interface, respectively. So, the study concentrated on the type of the driving forces should be done. For this study, it is very useful to

observe the same interface which has two kinds of driving forces which are clearly distinguishable respectively.

A magnetic domain wall (DW) has two distinct driving forces such as the magnetic field and the electric current. So, the DW owns suitability for studying the interface motions driven by different forces. The DW motion driven by the magnetic field has been well known in the last century. According to the researches, the field driven DW motion belongs to the universality class of the creep scaling. Recently, the current is known as another driving force of the DW. Despite of the short time to study the current driven DW motions, novel applications based on a wire geometry such as race track memory devices were suggested and then explosive studies are has being done. Among the properties of the current driven DW motion, the DW speed induced by the current determine the device operating speed thus, many researcher studied the speed of the DW. Recently, it was known that the current driven DW motion also belongs to the creep scaling just as the field driven DW motion.

If this result is true, the shape of the DW induced by the field and the current should be the same. However, there are no researches on the DW shape of the current driven case due to Joule heating problem. To solve this problem, we fabricate ultra clean perpendicular magnetic anisotropy (PMA) films. This films show clear circular

domains expansion by the field, implying that there are a few disorders and the film appropriate for studying the current driven DW motions.

Using these fabricated films, we investigate the uniaxial anisotropy constant of the PMA films with respect to the repetitions of multilayer structure. When the anisotropy constant is higher, the DW exhibits more clear morphology. We develop extraordinary Hall effect (EHE) probe and rotation stage for measuring the anisotropy constants then find out that the anisotropy constant has the maximum value at the one repetition of the PMA structure.

Next, we investigate the field driven DW dynamics. By using magneto-optical Kerr effect (MOKE) microscope, we measure the expansion and shrinking speed of the radius of the clear circular domains. We find out that there exists a long-range tension effect which is induced by the DW energy density.

We also investigate the electric current driven DW motions with circular and linear DWs. Quite interestingly, the DW speed depends on the DW tilting angle with respect to the current directions. From the angle dependence of the DW speeds, fully two dimensional DW driving equation with field and current was established.

Finally, we measure the DW motion in long-time range. Surprisingly, the current driven DW forms facet-like geometry and the speed of the DW drastically reduce after facet formation. But, the field

driven DW shows a smooth shape with a constant speed. This discordance comes from the sign of the nonlinear coefficient of the motions.

All of our findings enhance the fundamental understanding of the universality class with different driving force and also, provide technological as well as theoretical foundation to the novel devices based on DW motions.

Keywords: driving force, magnetic domain, domain wall, facet, creep, spin transfer torque, perpendicular magnetic anisotropy

Student number: 2006-20326

Table of Contents

Abstract ..... **ii**

List of Figures ..... **viii**

List of Table ..... **xi**

1 Introduction **12**

2 Development of experimental technic **16**

2.1 Optical technic 17

2.2 Electrical technic 25

3 Anisotropy constant of PMA film **27**

3.1 Stoner-Wohlfarth single domain theory and anisotropy constant 29

3.2 Measurement of magnetization tilting angle 32

3.3 Anisotropy constant with respect to repetition of PMA layer 34

4 DW energy density of PMA film **36**

4.1 Circular DW motion driven by magnetic field 37

4.2 Effective field induced by DW tension and dipolar field 45

4.3 Domain wall energy density 48

5 Generalized DW dynamics in fully two dimension **50**

5.1 Shape transformation of DW driven by electric current 51

5.2 Angle dependence of current driven DW motion 53

5.3 Generalization of creep scaling in two dimension 55

5.4 Origin of angle dependence 60

6 Facet formation and universality class transition 61

6.1 Pattern formation driven magnetic field and electric current 62

6.2 DW Pattern transition 67

6.3 Universality class of DW motion driven by field and current 70

7 Conclusions 71

Appendix 73

References 80

Author's Biography 89

Abstract in Korean 97

List of Figures

Figure 1.1 Perpendicular magnetic anisotropy film 14

Figure 2.1 Shematic diagram of MOKE microscope setup 18

Figure 2.2 Typical hysteresis loop of PMA film measured by the MOKE microscope... 19

Figure 2.3 Typical image processes using circular domain. Original image, background subtracted image and black and white image 20

Figure 2.4 Radius of the circular domain of fig .2.3 with respect to the angle. The upper data shows typical digitizing error. Lower data obtained by fitting..... 21

Figure 2.5 Thermomagnetic writing setup and image writing 22

Figure 2.6 Schematic diagram of electric setup and sample stage 23

Figure 2.7 Typical hysteresis loop of the PMA film measured by the electric setup 24

Figure 3.1 The Fourier coefficients A_i with respect to α 29

Figure 3.2 The measurement geometry of the sample..... 30

Figure 3.3 The extraordinary Hall voltage V_{H} and normalized $\cos\theta$ with respect to the sweeping angle ϕ for the film with n=2.. 32

Figure 3.4 The Fourier coefficient A_2 with respect to the external field H for the films with different n.....33

Figure 4.1 The circular domain radius r with respect to the elapsed time t.....40

Figure 4.2 Speed v with respect to the domain radius r.....42

Figure 4.3 Local effective magnetic field H_{eff}.....44

Figure 5.1 Domain wall motion driven by the field and the current 52

Figure 5.2 Field and current driven DW motions with constant tilting angles.....54

Figure 5.3 Scaling behavior of the field driven domain wall motions ..56

Figure 5.4 Speed contour map with respect to the field and the current.....57

Figure 5.5 Various angles results and the angle definition 58

Figure 5.6 Origin of the angle dependence.....60

Figure 6.1 DW moving distances along fixed h direction. 63

Figure 6.2 Normalized moving distances measured along fixed h axis.....64

Figure 6.3 Typical DW patterns change driven by a constant field.....65

Figure 6.4 Typical DW patterns driven by a constant current 66

Figure 6.5 Magnetization changes induced by field and current. 66

Figure 6.6 Stabilized pattern of DW with different bias field 67

Figure 6.7 Facet angle with respect to applied field strength 68

Figure 6.8 Typical pattern of DW when the field assists DW motion driven by current..... 69

List of Tables

Table 3.1 The anisotropy field H_K, perpendicular magnetic anisotropy K_U, and the coercive field H_C of the CoFe/Pt multilayers with different number of repeat *n*. 35

Chapter 1

Introduction

Magnetic domains in the magnetic material are certain areas which have uniform magnetization direction [1,2]. At the position of the dividing line of neighboring domains, the magnetization direction alters from one direction to the other direction and the dividing line is called as a magnetic domain wall (DW). It has been well known that the magnetic field moves the domain walls. And there are many researches on the field driven domain wall dynamics on the film geometry [3-5] as well as wire geometry [6-8].

Recently, it was discovered that the DW has another driving force. The second driving force is the electric current. The current drive DWs and this phenomenon is called “spin transfer torque (STT) effect” [9-12]. STT has two parts such as adiabatic STT and non-adiabatic STT. The adiabatic part has the origin on the process that the direction of the spin of the conduction electron and the direction of the local magnetization always parallel similar to adiabatic process. But the non-adiabatic part comes from the process that the spin direction of

conduction electron strays from the local magnetization directions. Then LLG equation with STT term show as below.

$$\frac{\partial \overrightarrow{M(t)}}{\partial t} = -\gamma_0 \vec{M} \times \overrightarrow{H_{eff}} + \frac{\alpha}{M_S} \vec{M} \times \frac{\partial \overrightarrow{M(t)}}{\partial t} - \underbrace{\frac{b_J}{M_s^2} \vec{M} \times (\vec{M} \times \frac{\partial \vec{M}}{\partial x})}_{\text{Adiabatic}} - \underbrace{\frac{c_J}{M_s} \vec{M} \times \frac{\partial \vec{M}}{\partial x}}_{\text{Non-adiabatic}} \quad (1.1)$$

Despite of the lateness of STT discovering, there has be done so many works on STT due to STT provide a new door to next-generation memory and logic devices based on a wire geometry [13-16]. So, STT studies were concentrated on the wire geometry and the DW in the wire geometry deals with single parameter to represent the DW position in the wire. However, DW is an interface rather than a point particle. So, interfacial study of DW should be done for all of the DW applications.

To study the interfacial motion of the DW, we select perpendicular magnetic anisotropy (PMA) films as samples (Fig. 1.1). PMA films are optimized to study the interface motion of the DWs because there exist only two types of domains (up and down) and the DW clearly formed at the boundary of different domains.

In **Chapter 2**, we develop two technics—electrical and optical methods for measuring properties of PMA films. The electrical method is based on the extraordinary Hall effect (EHE) and the optical method

is based on the magneto-optical Kerr effect (MOKE). In **Chapter 3**, we optimize the repetition of PMA layers by using the EHE probe to maximize the anisotropy for clear DW motions. The optimized film shows clear circular domain expansion induced by the magnetic field. To investigate interfacial motions of the DW, MOKE microscope with a charge-coupled device (CCD) camera measures the magnetization states of the PMA film. In **Chapter 4**, we measure the DW energy density from circular domain motions which is the basic parameter of the DW. **Chapter 5** shows the speed dependence of current driven DW motion on the DW angle and also shows both field and current belong to same universality class. In **Chapter 6**, the DW morphology with different driving forces such as the field and the current are quite

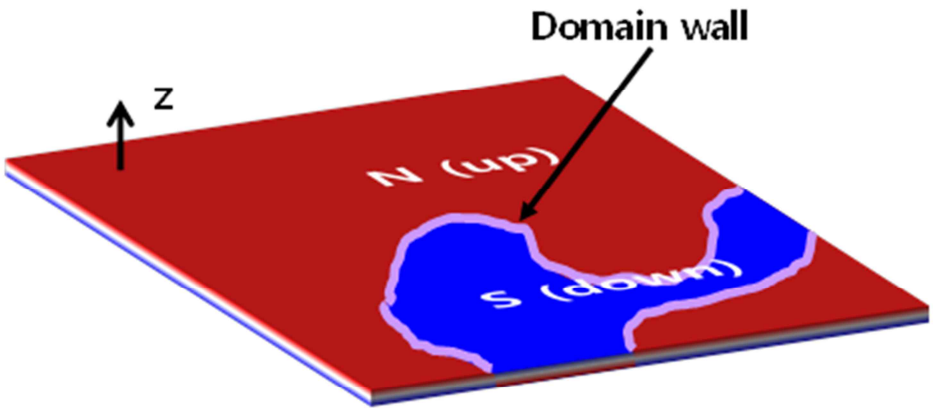

Figure 1.1 Perpendicular magnetic anisotropy film. There are two types of domains and domain wall are formed at the boundary of different domains.

different, especially current driven DW transforms facet-like geometry and we discuss the universality classes of the DW motions.

Chapter 2

Development of experimental technics

This chapter describes development of two measurement technics. The first technic is optical method that can visualize magnetization states of the PMA films. To investigate interfacial motion of the DW, it is necessary to observe large area in same time. So we developed a magneto-optical Kerr effect (MOKE) microscope with a charge-coupled device (CCD) camera and described in **Section 2.1**. Image processing method and thermomagnetic writing method are also explained. The second method is electric method using typical voltage measurement with current flow through the sample. In **Section 2.2**, we briefly explain the electrical measurement setup.

2.1 Optical measurement technic

2.1.1 Development of MOKE microscope

Figure 2.1 shows a schematic diagram of the MOKE microscope with a CCD camera. The microscope (Carl Zeiss, Axiotech vario) has mercury vapor short-arc lamp as a light source. The lamp exhibits light intensity with ~100 W and has the maximum power peak at the wave length 365 nm and in 436 nm at visible light range. Several Objective lenses (Carl Zeiss, Epiplan-Neofluar) with several magnification ranges from 100× to 2.5× provide various observation ranges of space. The light passes through the polarizer then the light has liner polarization. The polarization of reflected light form magnetic material is rotated due to the MOKE and the rotation depends on the surface magnetization. The transmittance through an analyzer is varied by magnetization state of the sample. Especially, the PMA film has two (up and down) domains and shows signal difference according to the magnetization states. The images are directly captured by the charge-coupled device (CCD) camera placed at the focal plane of the microscope. We used a CCD camera (Samsung, SHC-745) which is

very sensitive to the light difference thus optimized to measure the MOKE signal. Obtained image with typical video rate (~image/ 33ms) directly transfers to a computer and passes through the image processing such as subtracting background signal and averaging images. To apply the magnetic field, we made an electromagnet with a bipolar power supply (Kepco, BOP 50-4). The maximum field generated by the magnet is ~600 Oe (without iron core) and ~2300 Oe (with iron core).

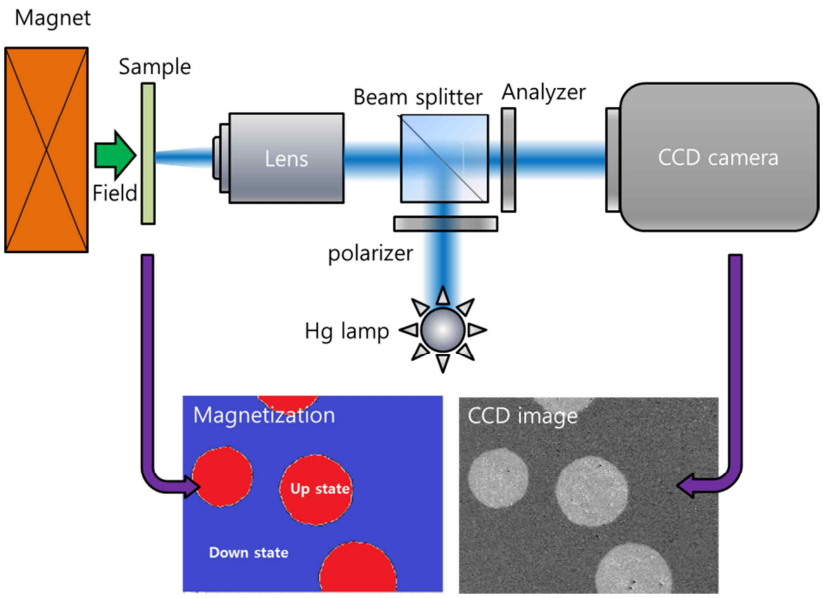

Figure 2.1 Shematic diagram of MOKE microscope setup.

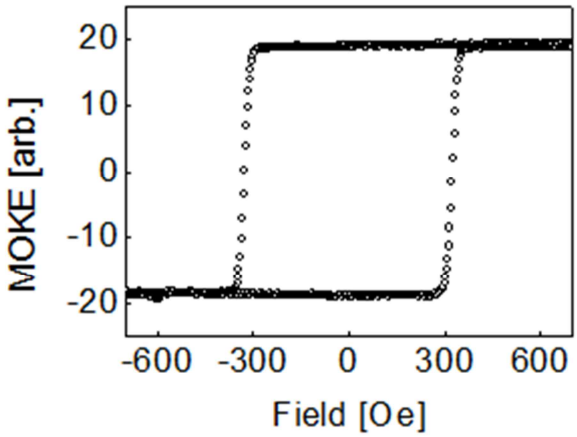

Figure 2.2 Typical hysteresis loop of PMA film measured by the MOKE microscope.

2.1.2 Method of image processing

- Background signal subtraction

PMA film has two stable magnetization states such as up and down. We obtain two magnetization images after saturation, respectively. And then we normalized the magnetization image using two saturation images. Figure 2.3 show typical image normalization of the circular domain. After normalization, we can cutoff the value to produce a black and white image.

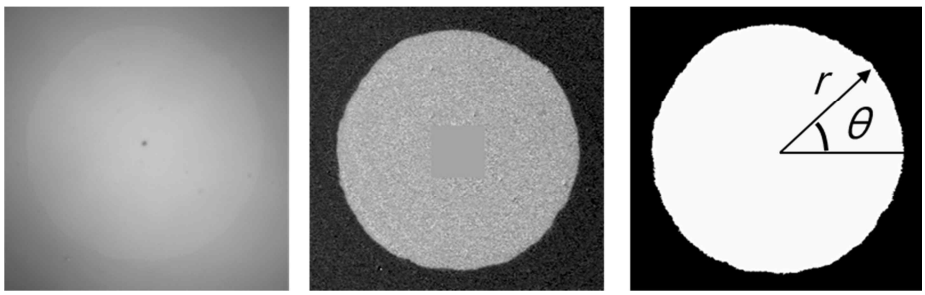

Figure 2.3 Typical image processes using circular domain. Original image (left), background subtracted image (middle) and black and white image (right).

- Finding DW position

It is important to find out the DW position exactly for the DW shape observation. We employ two methods to find the DW position. The first method started from black and white image. Each pixel data was compared with nearest neighboring pixel data. If at least one data is different we assume that there exists DWs. This method simple and past but obtained wall position has relatively large error range (~2 pixel of the image). Figure 2.4 shows the radius finding of the circular domain wall. Obtained radius with respect to the angle shows typical digitizing error. The second method is wall position finding by fitting. We extract the pixel data along fixed axis and the data are fitted by a tangent hyperbolic function. The function has transition value near the DW position. This method is more accurate but spends more time for fitting.

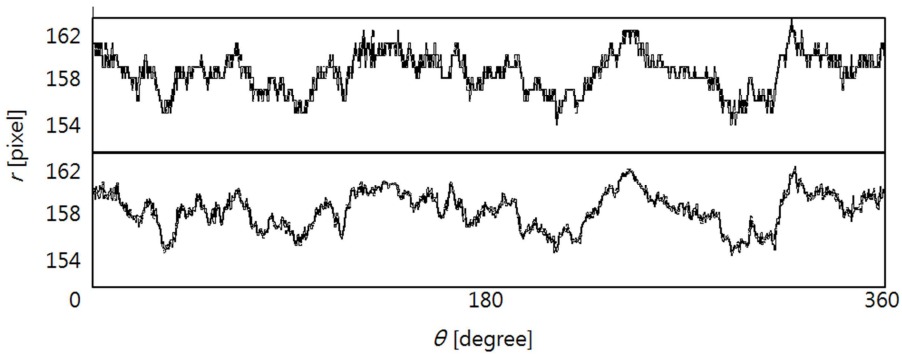

Figure 2.4 Radius of the circular domain of fig .2.3 with respect to the angle. The upper data shows typical digitizing error. Lower data is obtained by fitting.

2.1.3 Thermomagnetic writing

We develop a powerful technic for studying the DW motion in the PMA film. Arbitrary shaped domains formed by a writing method. This method based on thermally assisted magnetization reversal process. A focused laser beam heats the PMA film in the focused region. Heated area of the film increases temperature. If the temperature increase is sufficiently large, the magnetization can easily reverse at the low biased magnetic field. So there are formed a small region with reversed magnetization. Using writing method and motorized X-Y stage, we can write arbitrary domains. Figure 2.5 shows a schematic diagram of a writing setup and a writing result.

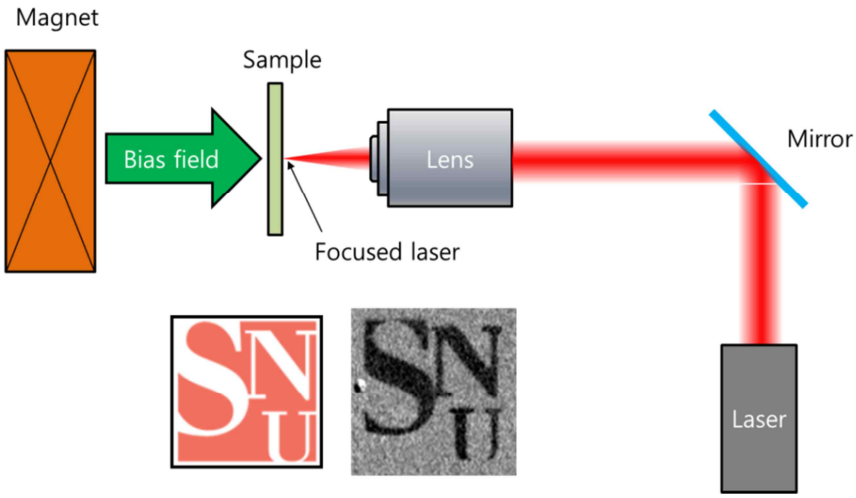

Figure 2.5 Thermomagnetic writing setup and image writing.

2.2 Electrical measurement technic

Electric measurements are widely used to detecting magnetization states of the sample because there are several electro-magnetic interaction such as anisotropic magneto resistance [17-20], extraordinary Hall effect [21], and giant magneto resistance [22,23]. So, we also develop electric measurement equipment which mainly composed by a single axis electromagnet, electric measurement parts and rotation stages. The homemade electromagnet with iron core generate magnetic field up to 2300 Oe with a bipolar power supply (Kepco, BOP 50-4). The electric part is composed with a current source (Keithley, 6221) and a voltmeter (Keithley, 2182A). Figure 2.5 show a schematic diagram of setup and a rotation stage. The rotation stage has

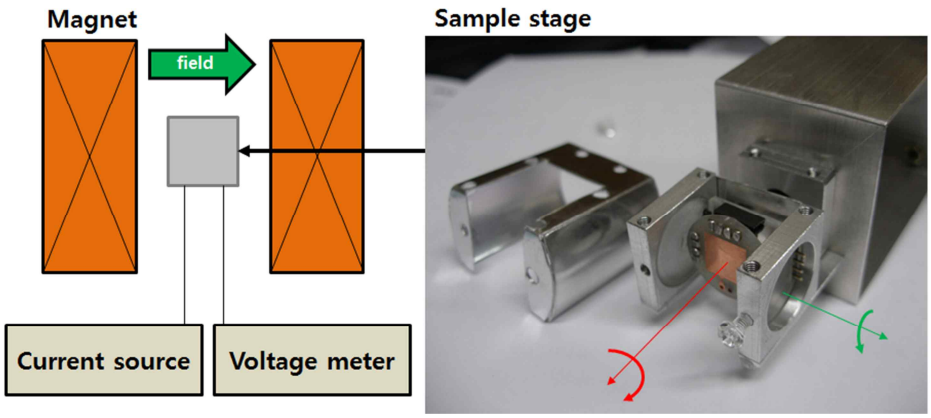

Figure 2.6 Schematic diagram of electric setup and sample stage.

two independent rotation axes. One axis connected to a motorized rotation stage and the other axis can be rotated in manually. By using two rotation axes, the magnetic field with arbitrary direction can be applied to the sample.

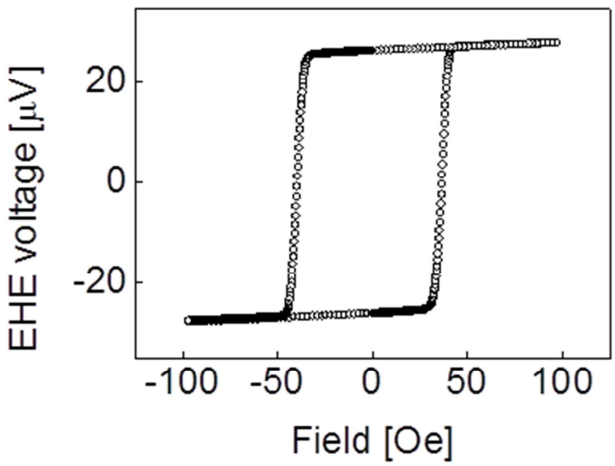

Figure 2.7 Typical hysteresis loop of the PMA film measured by the electric setup.

Chapter 3

Anisotropy constant of PMA film

Thin ferromagnetic films which have perpendicular magnetic anisotropy provide perspective challenges in high density data storage applications such as the hard disk [24,25], the spin-transfer-torque random access memory [26], the racetrack memory [13,27], etc. The static and dynamic properties are essentially influenced by the strength of the anisotropy in these materials and thus, precise measurement of the anisotropy is of importance to design and optimize the device performance. However, since most of the films with the perpendicular magnetic anisotropy are realized in ultrathin layered structures typically with a-few-angstrom thickness [28-30], it is hard to detect the weak signal from the small volume, by use of the conventional bulk techniques such as the torque magnetometry and the ferromagnetic resonance. In addition, the films with the perpendicular magnetic anisotropy generally exhibit complex magnetization reversal behaviors in competition between the wall motion and the nucleation, other than the coherent rotation [31-33]. It is thus hard to extract the sole

information of the anisotropy from the complex magnetization process.

In this chapter we propose a simple experimental technique to measure the perpendicular magnetic anisotropy field. The technique is based on the extraordinary Hall effect measurement, which preserves strong signal even in ultrathin films thus the effect is used as a useful tool for measuring the magnetization state [34]. The extraordinary Hall voltage is monitored with rotating an external magnetic field in a small angle around the easy axis and then, analyzed based on the Stoner-Wohlfarth theory with small angle deviation to extract the value of the anisotropy field. We confirm the perfect consistency between the experimental data and the theoretical prediction, which evidences the validity of the technique and consequently, provides the precise experimental value of the anisotropy field.

Section 3.1 represents theoretical description of Stoner-Wohlfarth theory and the anisotropy constant. **Section 3.2** shows measurement of magnetization angle by EHE measurement system. **Section 3.3** devotes to exhibit the results of the anisotropy constant variation of repetitions of PMA layers.

3.1 Stoner-Wohlfarth single domain theory and anisotropy constant

The extraordinary Hall voltage is monitored with rotating an external magnetic field in a small angle around the easy axis and then, analyzed based on the Stoner-Wohlfarth theory with small angle deviation to extract the value of the anisotropy field. We confirm the perfect consistency between the experimental data and the theoretical prediction, which evidences the validity of the technique and consequently, provides the precise experimental value of the anisotropy field.

For a magnetic system with uniaxial magnetic anisotropy, the magnetic energy E of the system is given by $E = -K_{\mathrm{U}} \cos^2\theta - M_{\mathrm{S}} H \cos(\theta - \phi)$, as first proposed by Stoner and Wohlfarth [35]. Here, K_{U} is the uniaxial anisotropy, M_{S} is the saturation magnetization, and H is the external field. The angles θ and ϕ are the angles of the magnetization and the external field from the easy axis, respectively. Note that the easy axis is normal to the film for the case of the perpendicular magnetic anisotropy. Normalized by K_{U}, the equation is rewritten as $\varepsilon = E / K_{\mathrm{U}} = -\cos^2\theta - 2\alpha\cos(\theta - \phi)$ with a single characteristic parameter $\alpha = M_S H / 2K_U$. The

equilibrium angle of the magnetization is then determined by $\partial\varepsilon/\partial\theta = 0$ i.e. $\sin 2\theta + 2\alpha\sin(\theta - \phi) = 0$. The equation provides multi-case solutions of $\theta(\alpha, \phi)$ depending on the initial condition, as given by Ref. [36] or readily solved by use of *Mathematica*. For heuristic purpose, we solely focus here on the case of $\phi \sim 0$ and $\theta \sim 0$, from which the other case of $\phi \sim \pi$ and $\theta \sim \pi$ can be easily derived by the symmetry argument. For small ϕ and θ, the solution can be written by the Fourier series expansion as $\cos\theta = 1 + A_2\phi^2 + A_4\phi^4 + A_6\phi^6 + \cdots$, where the Fourier coefficients are given by

$$\left.\begin{aligned} A_2(\alpha) &= \frac{\alpha^2}{2!(1+\alpha)^2} \\ A_4(\alpha) &= \frac{\alpha^2(4 - 15\alpha^2 + \alpha^3)}{4!(1+\alpha)^5} \\ A_6(\alpha) &= \frac{\alpha^2(16 - 54\alpha - 300\alpha^2 + 260\alpha^3 + 945\alpha^4 - 174\alpha^5 + \alpha^6)}{6!(1+\alpha)^8} \end{aligned}\right\}. \quad (3.1)$$

Figure 3.1 shows the Fourier coefficients with respect to α. As clearly seen from the figure, the higher order coefficients are negligibly smaller than A_2. It is thus quite reasonable to put the asymptotic solution as

$$\cos\theta \cong 1 + \frac{(M_S H)^2}{2(2K_U + M_S H)^2}\phi^2, \qquad (3.2)$$

for fairly wide range of ϕ. In the experiments we restrict $|\phi| \le \pi/6$ to avoid the switching of the magnetization. We confirm that inclusion/exclusion of the fourth order term A_4 does not make any noticeable change in comparison with the experimental accuracy.

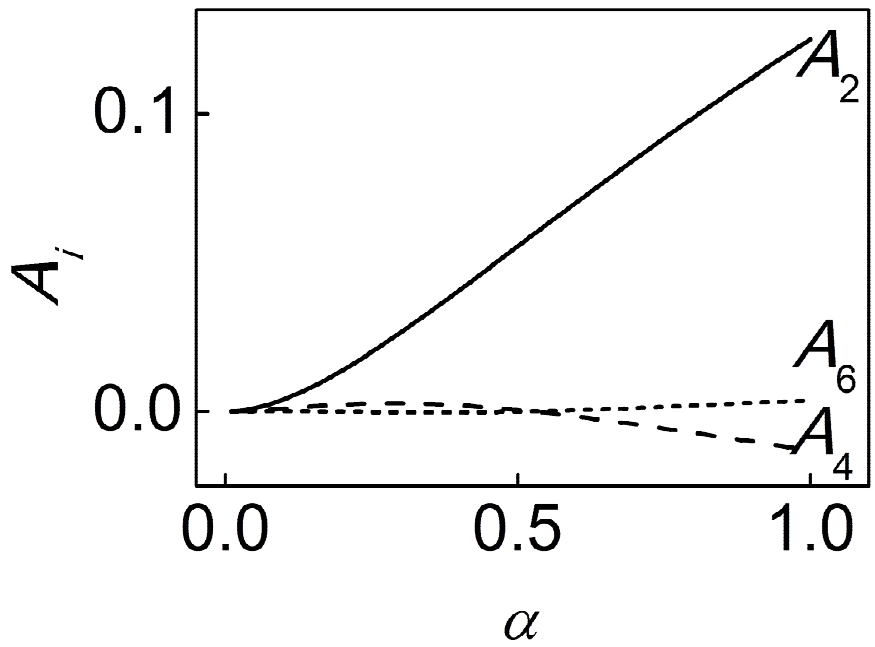

Figure 3.1 The Fourier coefficients A_i with respect to α.

3.2 Measurement of magnetization tilting angle

The magnetization angle θ is experimentally measured by means of the Hall effect. In the measurement setup, four wires are bonded at each corner of square-cut samples. One pair of diagonal corners is connected to the current source and the other pair is used for the voltage probe suggested as van der Pauw method [37]. However, in our experiment, it is not important to measure the exact value of the Hall voltage, so the electric connections make no significant problems. Figure 3.2 shows the wire connections of the samples. When a constant current 10 mA flows, transverse electric voltage is induced by

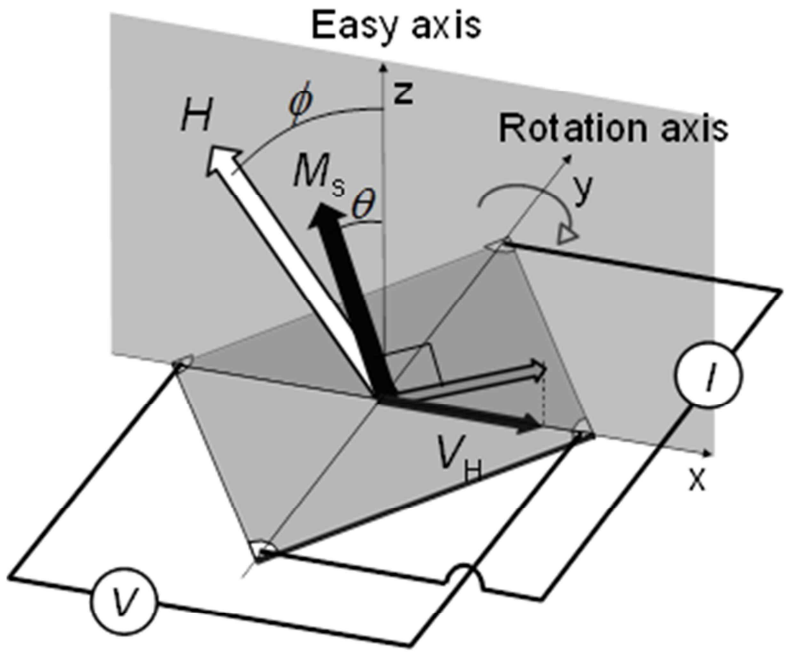

Figure 3.2 The measurement geometry of the sample.

the Hall effect. The Hall voltage V_{H} is expressed as $V_{\mathrm{H}} = R_{\mathrm{o}} I H_{\mathrm{z}} + R_{\mathrm{s}} I M_{\mathrm{z}}$, $H_{\mathrm{z}} = H\cos\phi$, and $M_{\mathrm{z}} = M_{\mathrm{s}}\cos\theta$. R_{o} is the ordinary Hall coefficient, R_{s} is the extraordinary Hall coefficient, and I is the current flow in the sample [38]. The voltage probes thus detect the out-of-plane components of the magnetization and the external field, which are proportional to $\cos\theta$ and $\cos\phi$, respectively.

To measure ϕ-dependence of the magnetization angle θ, a constant external magnetic field is applied normal to the film and then, the film is rotated by ϕ with the rotation axis, parallel to the current flow. In this method, the ordinary Hall voltage can be easily subtracted. During one rotation of ϕ from -180° to 180°, the ordinary Hall effect generates the signal proportional to $H\cos\phi$. The amplitude of the ordinary Hall voltage linearly depends on the external field. Hence, we can exactly subtract the ordinary Hall voltage by measuring with different applied fields. However, in realistic cases, the ordinary Hall effect is negligible because it is much smaller than the extraordinary Hall effect due to $R_{\mathrm{o}} << R_{\mathrm{s}}$ and $H < M_s$. Finally, one readily calibrates $\cos\theta$ after normalization with the relation, $\cos\theta = \{V_{\mathrm{H}} - (V_{\mathrm{Hmax}} + V_{\mathrm{Hmin}})/2\}/\{V_{\mathrm{Hmax}} - V_{\mathrm{Hmin}})/2\}$. V_{Hmax} and V_{Hmin} are the maximum and minimum values of V_{H} in the one round rotation measurement.

3.3 Anisotropy constant with respect to repetition of PMA layer

The present measurement technique is applied to CoFe/Pt multilayer films. 50-Å Ta/25-Å Pt/(5-Å $Co_{90}Fe_{10}$/10-Å Pt)$_n$ films are deposited on Si substrate with natural SiO_2 layer using dc-magnetron sputtering with changing the number of repeats n from 1 to 5 [39]. From the magneto-optical Kerr effect measurement, all the films are revealed to exhibit squared out-of-plane hysteresis loops, evidencing

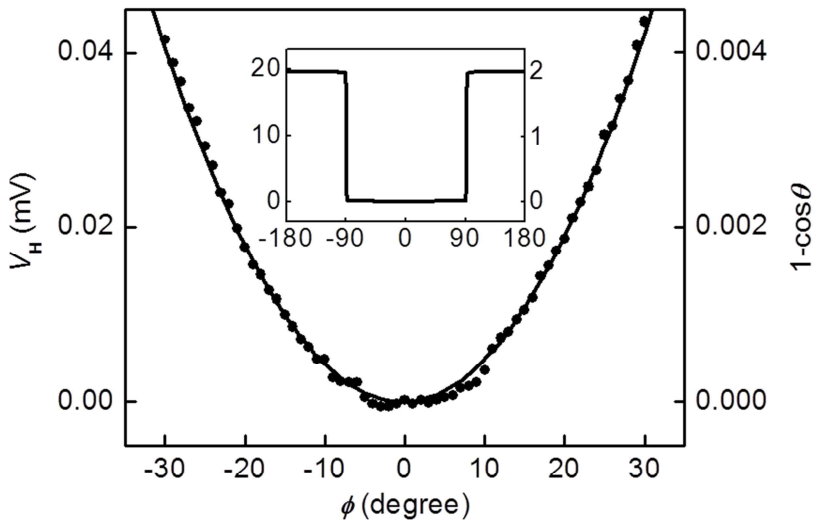

Figure 3.3 The extraordinary Hall voltage V_{H} and normalized $\cos\theta$ with respect to the sweeping angle ϕ for the film with n=2. The black line is the best fit with Eq. (3.2) by χ-square fitting. The magnetic field strength H is 200 mT.

the strong perpendicular magnetic anisotropy. The coercive field is monotonically increased with increasing n as listed in Table 3.1. The saturation magnetization M_S per Co volume is 2.0±0.2 T for all the films, measured by the alternating gradient magnetometer.

Figure 3.3 plots the extraordinary Hall voltage V_H with respect to the sweeping angle ϕ for the film with n=2. V_H is jump up and down at the angles -90° and 90° due to the magnetization reversal shown in the inset. The normalized value of $\cos\theta$ is shown

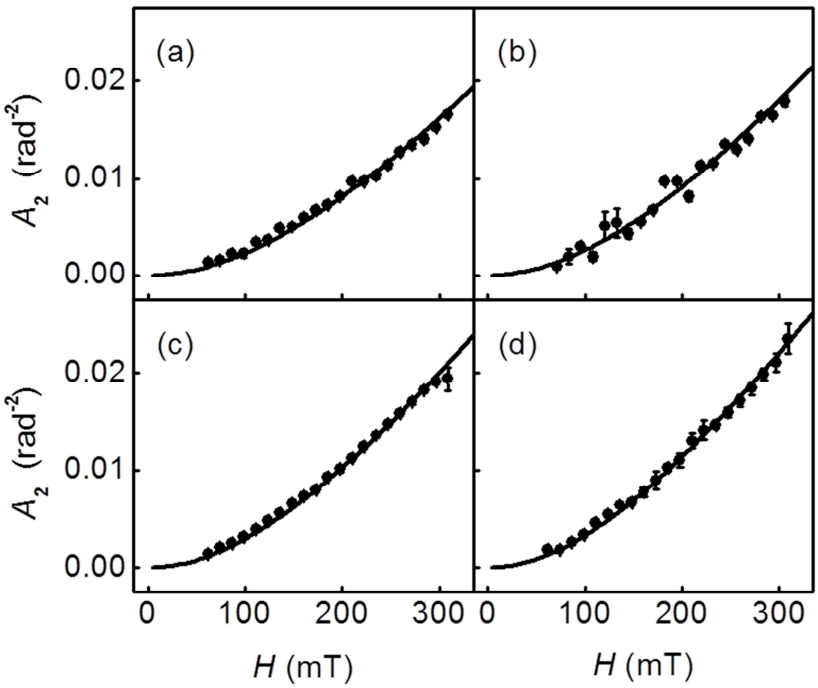

Figure 3.4 The Fourier coefficient A_2 with respect to the external field H for the films with different n—(a) 2, (b) 3, (c) 4, and (d) 5, respectively. The black lines are the best fits with Eq. (3.1).

in the right side of the plots. The rotation sense does not induce any noticeable changes near the angles 0° and 180°, which confirms that the magnetization process in this angle range is fairly reversible and therefore, compatible with the Stoner-Wohlfarth model. $\cos\theta$ is well fit to the parabolic function given by Eq. (3.2). From the best fit shown by the black line in figure 3, one can obtain the Fourier coefficient A_2. The coefficient is then converted to the anisotropy field H_{K} by

$$H_K \equiv \frac{2K_{\mathrm{U}}}{M_{\mathrm{S}}} = H\frac{1-\sqrt{2A_2}}{\sqrt{2A_2}}, \tag{3.3}$$

or to the uniaxial anisotropy K_{U} if the value of M_{S} is provided. The Fourier coefficient A_2 is measured with respect to the external field H. Figure 3.4 shows $A_2(H)$ for the films with different *n*—(a) 2, (b) 3, (c) , and (d) 5, respectively. The solid line is the best fit by $A_2(H) = H^2/2(H_K + H)^2$ as given by Eq. (3.1). The absolute conformity verifies the validity of the present measurement technique, as well as provides fairly reliable values of H_K. The experimental values of H_K and K_{U} are summarized in Table 3.1. The perpendicular magnetic anisotropy is found to be monotonically decreased with increasing *n*. It is possibly ascribed to the accumulation of the CoFe/Pt interfacial irregularities such as atomic misfits, defects,

dislocations, and crystalline misorientations with increasing the number of layers.

n	H_K (T)	K_U (10^6 J/m^3)	H_C (mT)
1	1.39±0.16	1.11±0.25	11.3
2	1.37±0.03	1.09±0.13	27.2
3	1.28±0.05	1.02±0.15	29.5
4	1.20±0.02	0.96±0.12	36.0
5	1.13±0.01	0.90±0.10	36.3

TABLE 3.1. The anisotropy field H_K, perpendicular magnetic anisotropy K_U, and the coercive field H_C of the CoFe/Pt multilayers with different number of repeat *n*.

Chapter 4

DW energy density of PMA film

This chapter is devoted to reviews the field driven DW dynamics, especially circular domain. The circular domain wall expansion and shrinking speed observation revels a long-range tension effect. From the tension effect, we can measure DW energy which is basic parameter of the DW.

Section 4.1 shows experimental result of circular domain motion driven by the magnetic field. It is clearly seen that a shrinking force exists on the circular domain wall motion. And the effective magnetic field obtained from the shrinking force exhibits inverse proportional to the domain radius. **Section 4.2** explains what the origin of the effective field is. The DW tension and dipolar field are the answer. And the DW energy density is rigorously determined from effective field and that is discussed in **Section 4.3.**

4.1 Circular DW motion driven by magnetic field

4.1.1 Introduction

Magnetic domain walls (DWs) in ultrathin films have recently attracted great technological attention due to the possible applications such as DW logic [14] and racetrack memory [13]. Up to now, the dynamic nature of DWs has been successfully analyzed by a rigid DW model [40,41] for magnetic-field- and/or current-induced DW motions related to intrinsic pinning [12,42] resonance frequency [40,43] and DW mass [40,44]. The DWs, however, inherently exhibit an elastic nature that minimizes the DW length because of a finite DW energy density σ_w. Such elastic nature is an important ingredient in the determination of the universality classes of the DW creep [4.8]. and Barkhausen [45,46] criticalities as well as the DW depinning field from geometric constraints [47,48] In the general sense, the elastic tension is known to exhibit a sizeable effect only for short-range distances. However, we report here a long-range elastic tension effect that subsists more than 20 μm from nucleation center. By observing circular domains expanding (or shrinking) under a constant magnetic field, a tension-induced magnetic field is measured that is inversely proportional to the radius of the circular domains. From the inverse

proportionality over a few tens of micrometers, σ_w is quantitatively estimated.

4.1.2 Experiment and result

For this study, Ta (50 Å) / Pt (25 Å) / Co (3 Å) / Pt (15 Å) films are deposited on a Si substrate with a natural SiO2 layer by dc-magnetron sputtering. The magnetization state as well as the magnetic domain images of these films is observed by a magneto-optical Kerr effect (MOKE) microscope equipped with an electromagnet. Figure 4.1(a) shows the polar MOKE hysteresis loop, which exhibits that the films have perpendicular magnetic anisotropy (PMA) with a small coercive field (30.0±0.5 Oe). These films exhibit magnetization reversal dominated by circular domain expansion. The domain dynamics is observed by the following procedure. A sufficiently large field (>300 Oe) normal to the film plane initially saturates the magnetization of the film and then, a reversed field is applied with a short rising time (<1 ms). When the applied field is larger than the coercive field, a reversed domain—formed at a natural nucleation site—expands circularly. After expanding up to a sufficiently large radius (but before coalescence to the adjacent domains), the applied field is reversed again to induce the domain shrinking motion. The polarity of the applied field is defined as positive when the applied field

is parallel to the magnetization of the circular domain. The expanding and shrinking domain images are observed in real time by the MOKE microscope. The images are directly captured with video rate by a charge-coupled device (CCD) camera placed at the focal plane of the microscope. The images are then processed by background subtraction (with the use of two positively/negatively saturated images) and noise reduction (with the use of a median filter). The observed domain is finally fitted by a concentric circle centered at the nucleation site, which enables us to measure the radius of the circular domain. Figure 4.1(b) shows a typical image of a circular domain. The dotted line (red) shows the circle with a radius r, centered at the nucleation site. Figures 4.1(c) and 4.1(d) show the domain radius r with respect to the elapsed time t after application of a magnetic field (±23.5 Oe) at t=0. In Fig. 4.1(c), after the nucleation of a domain at about 0.2 s, the domain expands in time. It is interesting to see from the figure that the domain expansion speed varies in time from zero to a typical value as guided by the dotted lines. Such speed variation in time is also observed in Fig. 4.1(d) for domain shrinking motion. These speed variations are universally observed at all the nucleation sites in the films, irrespective of the nucleation time that is determined stochastically by thermal activation for each nucleation site. Considering the time scale of these speed variations (about a few hundred milliseconds), they are irrelevant

to the domain-wall acceleration [49] under a constant magnetic field, which occurs within about a few nanoseconds. The field rising time (<1 ms) is also irrelevant since it is significantly faster than these speed variations.

We find that the speed variations depend on the domain radius

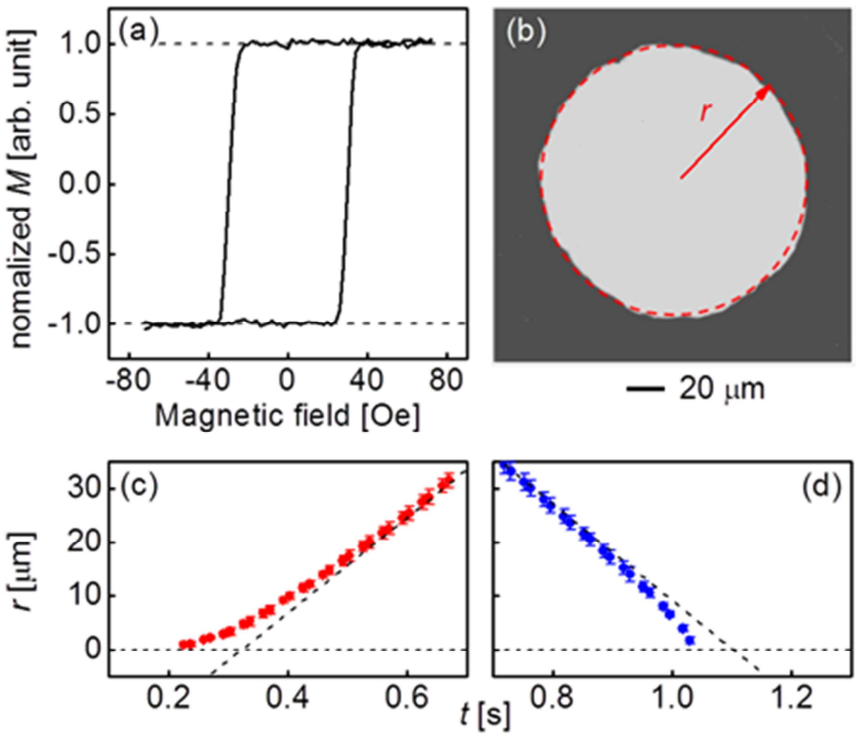

Figure 4.1 (a) Hysteresis loop measured by MOKE microscope with magnetic field normal to the film plane. The sweep rate is 1 Oe/s. (b) A typical domain image. The red circle shows the fitted circle with radius *r*, centered at the nucleation site. The circular domain radius r with respect to the elapsed time *t* for (c) expanding and (d) shrinking domain motions. The applied field is kept constant at +23.5 Oe for (c) and –23.5 Oe for (d). The dotted lines guide the constant speed at a large *r*.

rather than the elapsed time. Figure 4.2 shows the speed v—either expanding (red) or shrinking (blue)—with respect to the domain radius r. The speed v is measured from the subsequent two images with different radius r_1 and r_2 taken at t_1 and t_2, respectively, where $|t_2-t_1|$ is 33 ms. The speed v is then determined by $(r_2-r_1)/(t_2-t_1)$ and r is given by $(r_2+r_1)/2$. In the plot, different symbols indicate the results from several repeated measurements. It is clear from the figure that all the speeds with different symbols are collapsed onto a single curve as a function of r, for each expanding and shrinking motion. Note that, when the radius plotted with respect to time, as shown in Figs. 4.1(c) and 4.1(d), the repeatedly-measured $r(t)$ do not overlap onto each other, since the nucleation time varies stochastically for each measurement.

To explain the dependence of v on r, we first check v vs. H_{ext} relation for a large r regime. Figure 4.2 shows that with increasing r, the r dependence vanishes and v is saturated to a value v_s for both the expanding and shrinking motions. The inset of Fig. 4.2 summarizes the v_s vs. H_{ext} relation measured for r>50 μm. It is clear from the figure that the relation exhibits the well-known creep scaling [4] $\ln v_s = \ln v_0 + \alpha\{H_{ext}\}^{-1/4}$, where α is a field-independent constant related to the energy barrier and the thermal energy and v_0 is the characteristic speed.

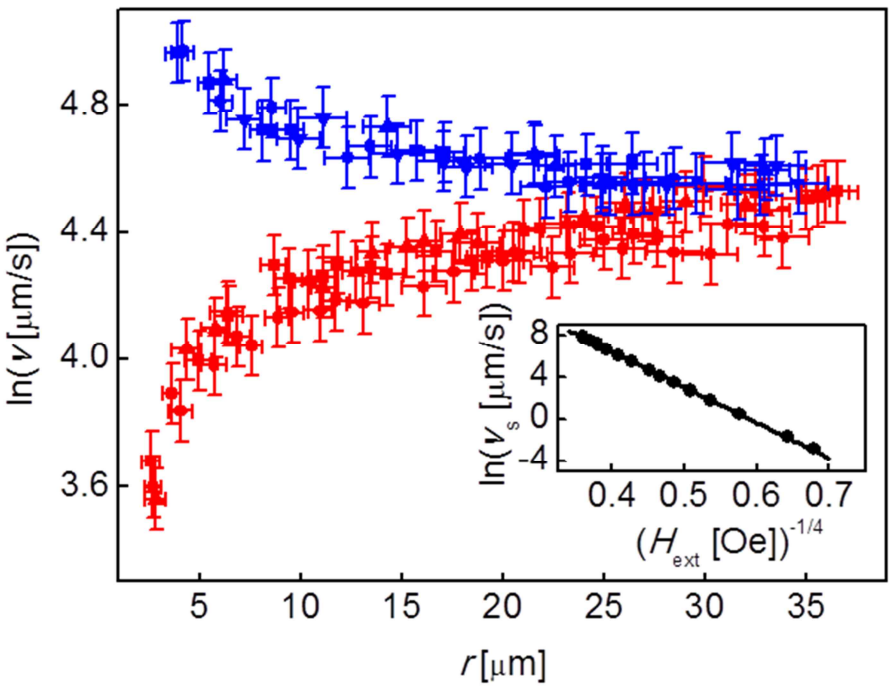

Figure 4.2 Speed v with respect to the domain radius r, for expanding (blue) and shrinking (red) motions. The different symbols indicate the results for each repeated measurement. Inset: Creep plot between ln v_s and $\{H_{ext}\}^{-1/4}$. The line shows the best linear fit.

From the best linear fitting, the values v_0 and α are determined to be 397 m/s and –33.7 $Oe^{1/4}$, respectively. On the other hand, for a small radius regime (r<30 μm), a clear r dependence is observed. Such r dependence possibly comes from the change in the disorder pinning potential [6] and/or the effective field [50]. The former is expected to be negligible because the disorder correlation length (~10 nm) as well as the Larkin length is significant shorter than the domain radius (>1 μm) in our experiments. Note that the curvature of the domain walls produces an arc length 0.001% longer than the straight line of ~10 nm length. We thus exclude the effect of the disorder pinning potential change and focus on the latter. To do this, we introduce a concept of the local effective magnetic field H_{eff} and we consider that the speed $v(r)$ is governed by the total magnetic field H_{tot} (=H_{ext}+H_{eff}). Then, the total magnetic field H_{tot} has the relation $\ln[v(r)]=\ln v_0 +\alpha\{H_{tot}\}^{-1/4}$, replacing H_{ext} in the typical creep equation. By use of $v(r)$ in Fig. 2, H_{tot} can be estimated by $H_{tot}(r)=(\{\ln[v(r)] - \ln v_0\}/\alpha)^{-4}$ with respect to r and finally, H_{eff} is determined by $H_{eff}(r)=H_{tot}(r)–H_{ext}$.

Figure 4.3 exhibits H_{eff} with respect to $1/r$ for various strengths of H_{ext}. It is very interesting to see that (almost) linear relations exist between H_{eff} and $1/r$, irrespective of H_{ext}. The shapes for the expanding and shrinking motions are identical except the sign (negative for expanding motion and positive for shrinking motion).

Note that H_{eff} induces a force to shrink the circular domain, since $H_{eff}>0$ for the shrinking motion and $H_{eff}<0$ for the expansion motion.

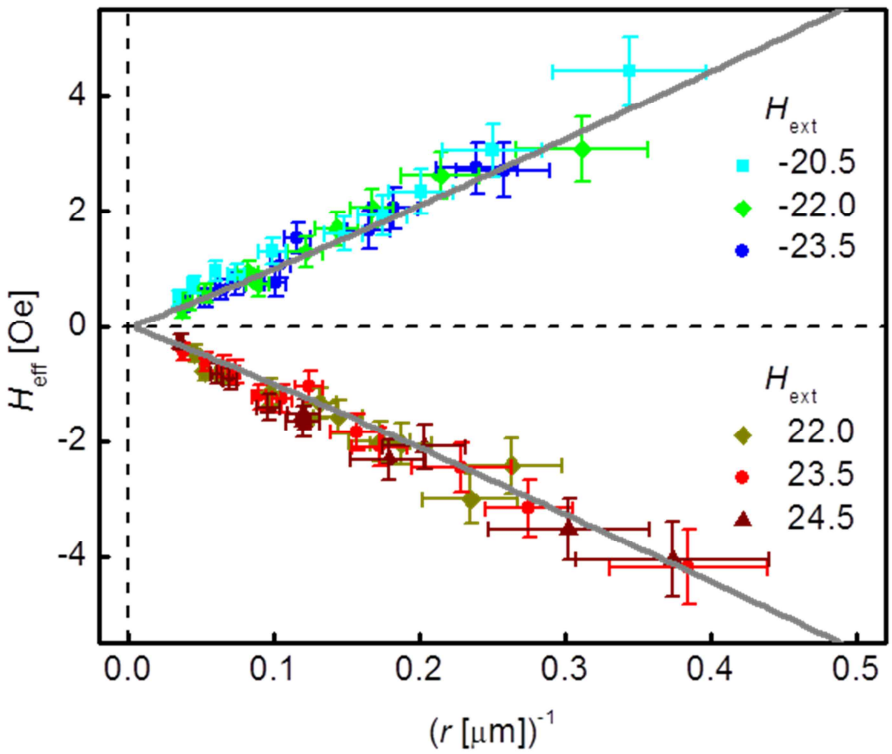

Figure 4.3 Local effective magnetic field H_{eff} with respect to the inverse of the radius r for various external magnetic fields H_{ext}. The gray lines show the best fit with effective field H_{eff} ($=H_w+H_d$).

4.2 Effective field induced by DW tension and dipolar field

The $1/r$ dependence in H_{eff} can be explained by the DW tension and the magnetostatic dipolar interaction. The DW tension is caused by the DW energy E_{w} due to the finite DW energy density ε_{d} per unit length. The effective magnetic field H_{w} induced by the DW tension is then defined as $H_{\text{w}}=-\delta E_{\text{w}}/\delta M$, where M is the total magnetization of the film. Here, δE_{w} and δM denote small changes of E_{w} and M, respectively. When a circular domain of the radius r expands concentrically by δr, δE_{w} is given by the change in the DW length as $\varepsilon_{\text{d}}(2\pi\delta r)$ and δM is given by the change in the domain area as $\pm(2M_{\text{S}}t_{\text{f}})(2\pi r\delta r)$. Here, M_{S} is the saturation of the magnetization and t_{f} is the film thickness. The sign indicates the polarity of the magnetization in the circular domain. The effective magnetic field H_{w} is then given by

$$H_{\text{w}} = \mp\frac{\varepsilon_{\text{d}}}{2M_{\text{S}}t_{\text{f}}r}, \tag{4.1}$$

which clearly shows a $1/r$ dependence on H_{w}. It is also worthwhile to note that the sign of H_{w} is always opposite to the magnetization of the

circular domains, acting as a tension to shrink the circular domain, in accordance with our experimental observations.

The magnetostatic dipole interaction also results in a quasi-1/r dependence of the effective field H_{eff}. Considering a circular domain of a radius r with a finite DW width λ and assuming that the magnetization inside the DW lies in the plane (i.e., no perpendicular component inside the DW), the out-of-plane component of the dipolar field H_{d} can be derived as $H_{\mathrm{d}}(r)=\pm(M_{\mathrm{S}}t_{\mathrm{f}}/r)F(\lambda/r,t_{\mathrm{f}}/r)$ at the center of the DW, where the dimensionless factor F is analytically given by $F(a,b)=[a^2+b^2]^{-1/2}-G^{+}(a/4,b/4)-G^{-}(a/4,b/4)$, where

$$G^{\pm}(a,b)=\frac{1}{4\pi}\int_{a}^{1\pm a} x\cos^{-1}(x\mp ax^{-1}-a^2x^{-1})/\left(x^2+b^2\right)^{3/2}dx\,. \qquad (4.2)$$

Since the domain radius r in this experiment is much larger than the film thickness t_{f} and the DW width λ, eq. (2) can be simplified by the Taylor expansion [51] with respect to t_{f} and λ, finally resulting in

$$H_{\mathrm{d}}(r)\approx\pm\frac{M_{\mathrm{S}}t_{\mathrm{f}}}{r}\left[\frac{1}{4}-\frac{7}{48\pi}+\frac{1}{2\pi}\ln\left(\frac{4r}{\lambda}\right)\right], \qquad (4.3)$$

which clearly exhibits quasi-1/r dependence. The value of the terms inside the parentheses of eq. (4.3) is less sensitive to r (in comparison

with $1/r$ outside the parentheses) and remains close to unity in our experimental situation. The sign indicates the magnetization polarity of the circular domain and thus, the dipolar field prefers to expand the circular domain, oppose to H_w.

4.3 Domain wall energy density

The local effective field H_{eff} in Fig. 4.3 is then analyzed by use of the relation $H_{eff}=H_w+H_d$. To do this, we assume the Bloch wall configuration in our films, since the Bloch wall has certainly lower energy than the Neél wall due to the narrow DW formation in our films. Replacing λ by $\pi\varepsilon_d/(4t_fK)$ based on the Bloch wall configuration, and by use of the experimental values M_S=1.6±0.2 T determined by an alternating gradient magnetometry (AGM), the anisotropy constant K=(8.3±0.2)×10^5 J/m^3 determined by an angle-dependent extraordinary Hall effect measurement [21], and t_f=0.3 nm, the data H_{eff} in Fig. 3 are fitted by the formula H_{eff} with a single fitting parameter ε_d as shown by the gray lines, resulting in the best fit value ε_d=(1.3±0.2)×10^{-12} J/m. In our Pt/Co/Pt films, the DW tension field H_w is found to be about 4 times larger than the dipolar field H_d. However, it is interesting to note that due to the different t_f-dependence of eqs. (4.1) and (4.3), H_d can be dominated in thicker films as well as there exists a critical thickness in which H_w and H_d are almost compensated, i.e., no local effective field.

The DW energy density per unit area σ_w (=ε_d/t_f) is finally determined to be 4.5±0.7 mJ/m^2, which is typical in Co and Pt based PMA films [52-59]. It is worthwhile to compare our experimental value σ_w with the Bloch wall energy formula $\sigma_w=4(AK)^{1/2}$ where A is

the exchange stiffness. By use of the experimentally determined values σ_w and K, the exchange stiffness A is estimated to be $(1.5\pm0.5)\times10^{-12}$ J/m, which is about one order smaller than the bulk value. Such reduction might be possibly caused by the formation of the fine polycrystalline grain boundaries in ultrathin magnetic films. It is worthwhile to note that for the case when all the grain boundaries have the similar properties, the pinning strength should be isotropic in large scale even though the DW exhibit roughness according to the grain boundaries in small scale. It is thus possible to form large regular circular domains even with large amount of polycrystalline grain boundaries.

In summary, we report an experimental observation of a long-range domain wall tension effect which subsists over 20 μm. The tension-induced field as well as the magnetostatic dipolar field is found to be inversely proportional to the radius of the circular domain, which enables us to directly determine the DW energy density.

Chapter 5

Generalized DW dynamics in PMA films

This chapter shows the first observation of angle dependences of the DW speed driven by electric current. From the angle dependence, we find out the generalized creep equation in fully two-dimensional system.

Section 5.1 shows brief experiment which exhibit the speed of the DW depends on the DW angle from the observation of the circular domain shapes transformation induced by the electric current. In **Section 5.2,** experiment with linear DWs is shown. **Section 5.3** reveals that generalized creep equation in full two-dimension. In **Section 5.4**, we discuss the origin of angle dependence.

5.1 Shape transformation of DW driven by electric current

Typical magnetic domain wall (DW) motions driven by the magnetic field are observed in **Chapter 4**. Now, we observe the current driven DW motions on the same PMA film. A domain with a small area ~15 × 15 μm^2 is formed by the thermomagnetic writing method at the film with saturated magnetization state (Fig. 5.1(a)). A constant magnetic field pulse with 35 mT in intensity, 500 ms in duration is applied to the film. After the field pulse, clear circular domain is formed (Fig. 5.1(b)). Another same field pulse is applied to the film then larger circular domain expands (Fig. 5.1(c)). Red dashed circles represent the domain wall positions of figure 5.1(a), (b). The center of the circles and the radius variations are identical. So, it is reasonable to assume that the domain wall propagate to the radial direction with the same speed. When the circular domain expansions are observed at the wall position, wall propagates to the normal direction of the wall itself. These propagation properties are basically due to symmetry of the film. Film is isotropic to any in-plane direction.

We inject the electric currents in the film and observe the magnetization state change. For current injection, gold electrodes deposited at the end of the film. The current pulse density in the film is

3.4 × 10^{10} A/m^2 and duration is 2 ms. Current flows to *h* direction. The current density is sufficiently small so that Joule heating problem is not significant [59-61]. According to the STT equation [9-12], circular domain wall shift to the direction of current flow with same distance at any positions of domain wall thus circular domain preserve its shape. However, amazingly, the circular DW transforms to a bullet shape. Figure 5.1(d), (e) show consecutive magnetization states of the film after injection of 100 times pulses to circular domain state (fig. 5.1(c)). Top position of domain, marked as A in Fig. 5.1, moves the longest distance along *h* direction and also bottom position C move same distance with A. However, edge positions B shows no DW motions. This drastic difference of moving distance at each DW position is the cause of the shape transformation.

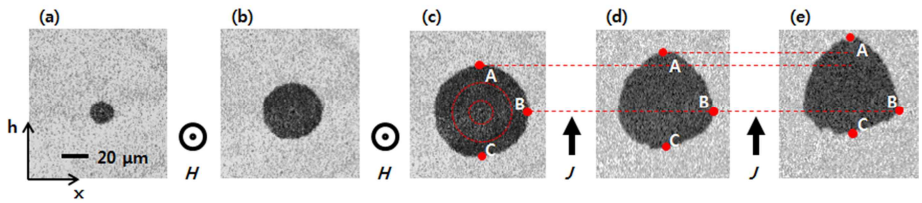

Figure 5.1 Domain wall motion driven by field (a)-(c) and driven by current (c)-(e).

5.2 Angle dependence of current driven DW motion

The current passes through the DW walls normally at the position A and C in Fig. 5.1 but parallel at position C. So we expect that the reason of distance difference is the DW tilting angle to the current direction. To verify this assumption, we write a linear DW with constant tilting angle. And we inject constant field or current pulse. From before and after images, we obtain the DW position and draw it in same image. Then moving distances of the DW by the pulse are directly shown. Figure 5.2 shows typical motions of linear domain walls with several constant tilting angles θ driven by constant field (35 mT, 300 ms) and current (7×10^{10} A/m^2, 0.12 ms) respectively. θ is the angle between h axis and the normal direction of the DW slope. The Field driven DW moves normally to the DW thus the motions are independent on the tilting angle. However, for the current cases, DW motion has apparent angle dependences. Current flows to h direction. As increase θ from 0° to 90°, the displacements of the DW monotonically reduces. From these results, we find out that the DW angle is an important parameter of the current driven DW motions.

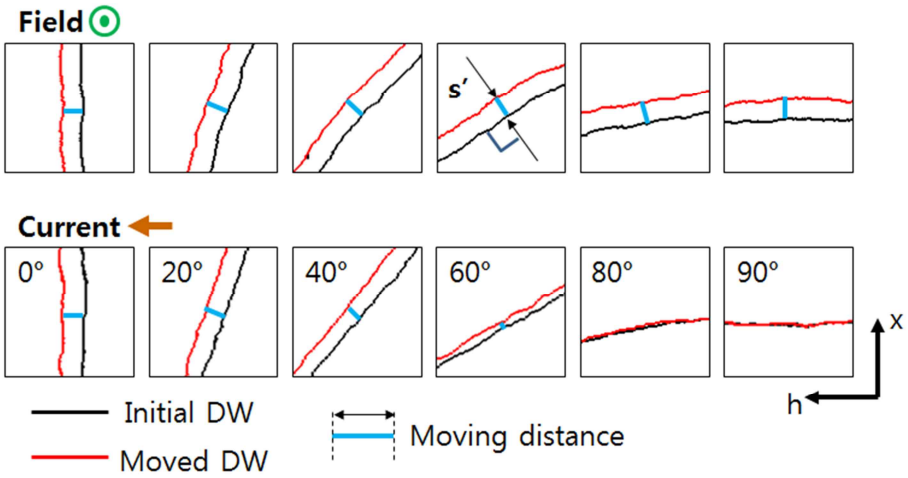

Figure 5.2 Field and current driven DW motions with constant tilting angles. Image size is 50μm x 50μm. Before and after DW positions are shown as black and red line, respectively. DW moving distance denoted by *s*' measured along perpendicular direction of the DW. *s*' is independent on the tilting angle in field cases. But current cases clearly show speed dependence on angle.

5.3 Generalization of creep scaling in two dimension

DW speed driven by magnetic field shows well known creep scaling behavior. For small field *H*, the effective energy barrier scales as power law $H^{-\mu}$ with creep exponent μ. Then the speed flows $v_H = v_0 exp\ (-\alpha H^{-\mu}/k_B T)$ due to Arrhenius law of thermal activation. v_0 is a characteristic speed, α is a scaling constant, and $k_B T$ is the thermal energy (see Appendix). Recently, Ryu *et al*. reveal that the electric current corresponds with the magnetic field in the DW motion [62,63]. Current density *J* and magnetic field *H* compose the Effective field *H** shown as,

$$H^*(H,J) = H - \not{\varepsilon} - \eta J^2 \sqrt{H - \not{\varepsilon}} + \frac{2}{5}(\eta J^2)^2 + \mathcal{O}(J^6) \qquad (5.1)$$

Here, ε and η are constants. And the speed flows creep law,

$$v(H,J) = v_0 \exp\left\{-\frac{\alpha[H^*(H,J)]^{-\mu}}{k_B T}\right\} \qquad (5.2)$$

This equation assumes that the direction of the electric current is perpendicular to the DW. So the moving direction driven by the

magnetic field and the electric current is always parallel in equation (5.2).

Firstly, we measure the field driven DW motions with the perpendicular DW ($\theta = 0^\circ$). We write linear DWs and then measuring the speed with constant magnetic field. Figure 5.3 shows perfect scaling behaviors of the field driven DW motion. Then we also measure the DW speed with several constant currents and fields. To compensate the Joule heating effect, we measure the temperature elevation at each current density and convert the measured speed V_m to adjusted speed V at the room temperature based on Arrhenius law and temperature dependent the field creep measurements. Figure 5.4 shows contour map of the DW speed as a function of field and current.

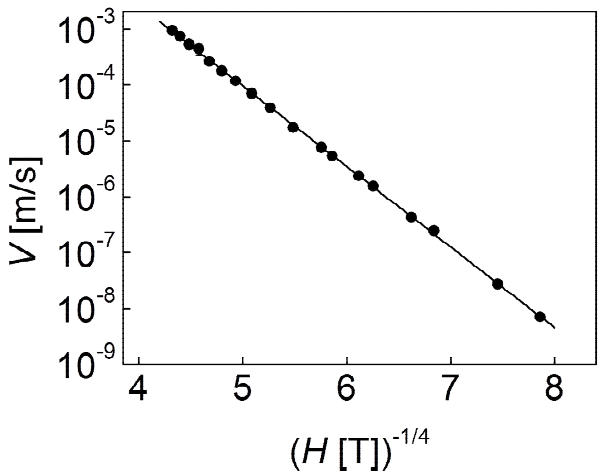

Figure 5.3 Scaling behavior of field driven domain wall motion. The line shows the best linear fitting line.

According to equation (5.1), equi-speed line in figure 5.4 written as $H = H^* + \mathcal{J} + \eta J^2\sqrt{H^*}$. To obtain the ε and η, we fitted equi-speed line. Then we find best fitting parameter $\varepsilon = -(1.8 \pm 0.1) \times 10^{-14}$ [Tm^2/A]. η is negligible in experiments current range so, we set $\eta = 0$. Then, certain magnetic field and electric current in figure 5.4 is easily converted to Effective magnetic field *H**. Figure5.5 shows clear creep scaling of DW speeds with respect to the effective fields. Through these processes, we verify generalized creep equation when DW moving direction and the current flow direction is parallel.

Next, we repeat same experiments with several DW angles. The DW speed is measured along perpendicular direction of the DW and measured speeds are fitted by the effective field *H** as,

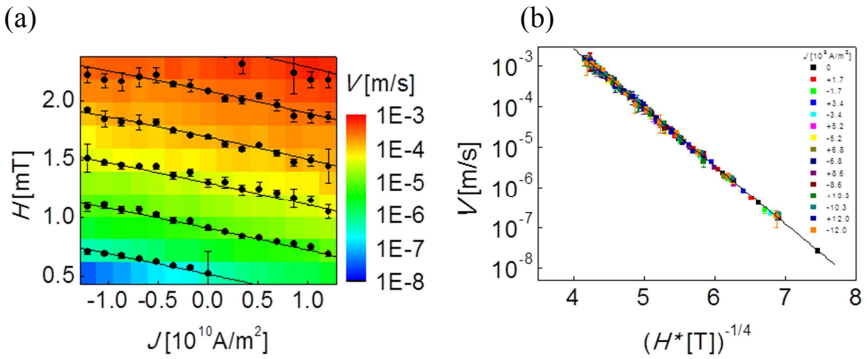

Figure 5.4 (a) Speed contour map with respect to field and current. Solid lines represent equi-speed lines which denote the effective magnetic field *H**is same. (b) Generalized creep scaling with respect to effective field *H**. All of the data in figure collapse to one single line.

$$H^*(H,J) = H - \epsilon\cos\theta\, J - \eta\cos^2\theta\, J^2\sqrt{H - \epsilon\cos\theta\, J}$$

$$+\frac{2}{5}(\eta\cos^2\theta\, J^2)^2 + \mathcal{O}(J^6).$$

(5. 3)

Figure 5.5 shows creep fitting of several angles. All of data collapse to the field creep curve shown in Fig.5.3. Surprisingly, when the DW are parallel to the current direction, effective field well meet to the field

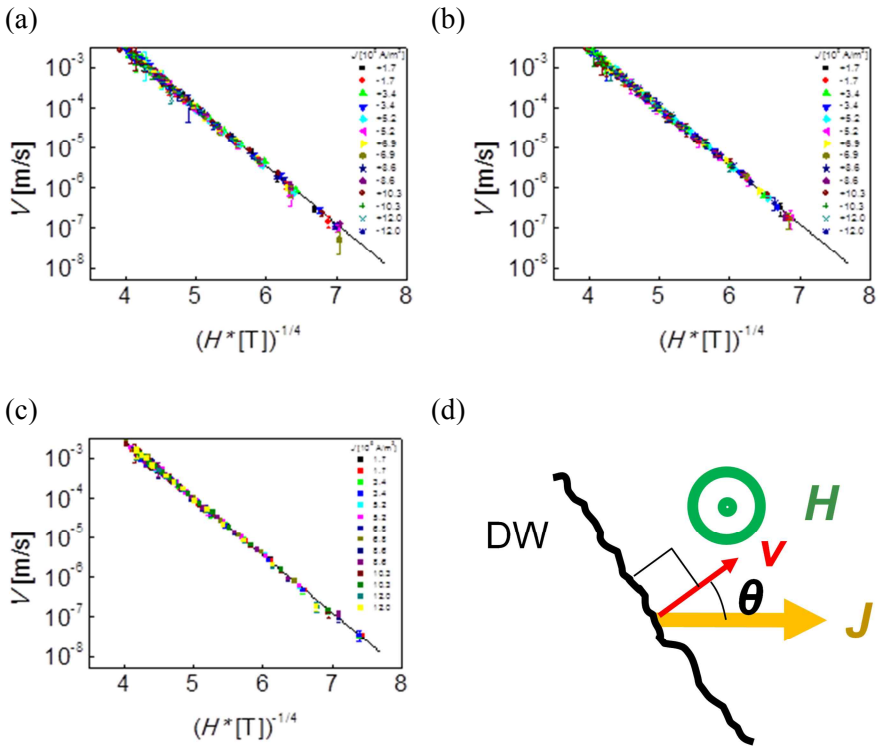

Figure 5.5 Various angle results (a) 30°, (b) 60°, (c) 0°. All of data are collapsed to the field creep result (black line). (d) Definition of angle of the DW and current. Measured speed direction is perpendicular to

creep case.

From these experiments, one can directly drive generalized 2-D creep equation with arbitrary shape or slope of DW. The current density J is replaced by $J\cos\theta$ or $\vec{J}\cdot\hat{n}$ in vector form. Here, $\hat{n}$ is normal direction of the DW. We rewrite (5.2) as a vector equation.

$$\vec{v}\left(H,\vec{J}\cdot\hat{n}\right)=v_0\exp\left\{-\frac{\alpha\left[H^*\left(H,\vec{J}\cdot\hat{n}\right)\right]^{-\mu}}{k_BT}\right\}\hat{n} \tag{5. 4}$$

We obtain generalized creep equation with arbitrary shaped DW in fully two dimensions.

5.4 Origin of angle dependence

The current can be separated by a perpendicular component and a parallel component to the DW. The parallel component cannot move the DW because the spin transfer torque is proportional to the magnetization gradient along current direction. Thus, parallel component of the current generate no STT to the DW. In addition to this zero STT, parallel motion of DW driven by parallel current is undistinguishable. So, we should think only the perpendicular current density which can generates distinguishable DW motion. The perpendicular current density is simply $J\cos\theta$.

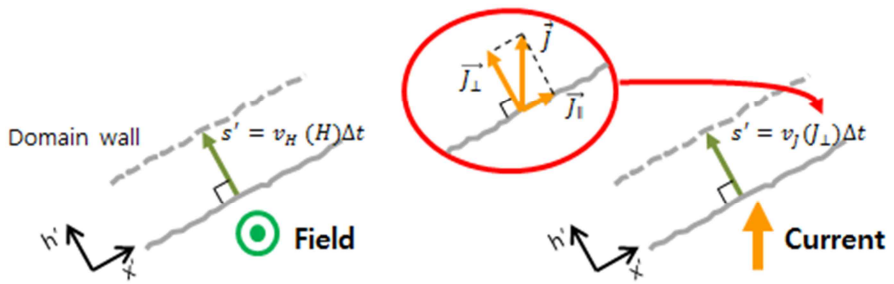

Figure 5.6 Origin of angle dependence. Perpendicular current density varied with respect to the angle of DW. Distinguishable motion of DW can be generated by only perpendicular current density.

Chapter 6

Facet formation and universality class transition

This chapter devote to the DW shape. We observe final pattern of DW driven by field and current, respectively. In field driven DW case, the DW exhibits ordinarily interface motion with smooth shape. But the current driven DW made facet pattern due to negative nonlinear term in interface growth equation.

Section 6.1 describes the DW patterns formation from initially linear DW. In **Section 6.2,** we investigate DW pattern transition with respect to the current and the field intensity. Universality classes of the DW motions are discussed in **Section 6.3**.

6.1 Pattern formation driven magnetic field and electric current

The DW motions can be approximately described by quenched Kardar-Parisi-Zhang (QKPZ) equation [64-68] because both the DW motion and QKPZ equation describe the motion of an interface in a disordered media. According to the QKPZ equation, interface high h at position x and time t is described by,

$$\frac{\partial h}{\partial t} = F + \nu \frac{\partial^2 h}{\partial x^2} + \frac{\lambda}{2}\left(\frac{\partial h}{\partial x}\right)^2 + \eta(x,h) \tag{6.1}$$

Where, ν is surface tension, λ is a coefficient of nonlinear term and η is noise term. Among these parameter, ν and η has the same value regardless of field and current driven cases because the wall energy and the quenched disorder have no dependence on the driving forces. However, λ depend on the type of the driving forces.

To find out λ, we obtain DW moving distances from Figure 5.2 once again. Rather than obtain moving distance along perpendicular direction to the DW, the distance measured along fixed axis parallel to the current direction. Figure 6.1 shows obtained moving distances. Field driven case exhibits increasing moving distance with respect to

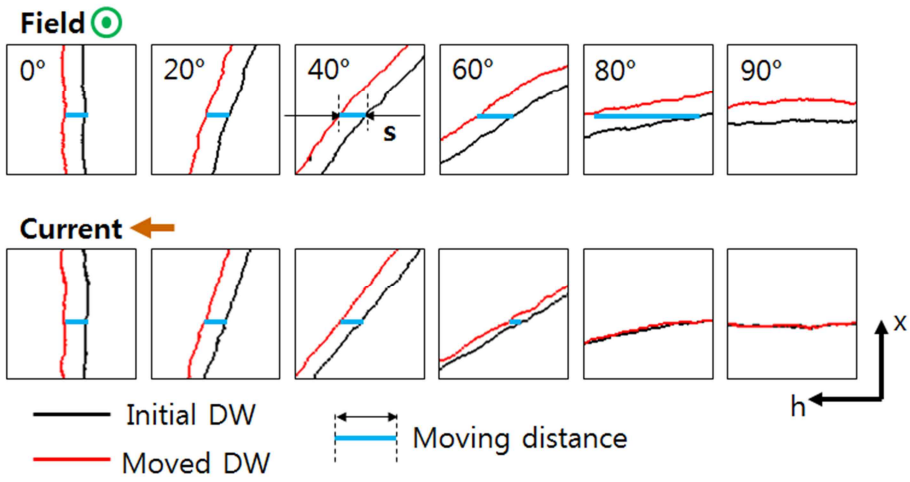

Figure 6.1 DW moving distances along fixed *h* direction.

the DW angle increase. It is a coordinate rotation effect. The current driven cases show decreasing moving distance when the angle increases despite of coordinate rotation effect. The moving distance dependence on DW angle shows clear opposite tendency according to the type of driving forces shown as in figure 6.2. Field driven case, the coefficient of nonlinear term is positive. But the current case, λ has a negative sign.

This opposite nonlinear coefficient induces different interface morphology. Figure 6.3 shows typical domain patterns driven by a constant field with initially linear DW (θ~0°). When the DW meet strong disorder during motion, the DW deformation occurs like a bowstring. Form the DW deformation, the DW has non zero θ near the pinned position. In the field driven DW motion, increase θ assists the

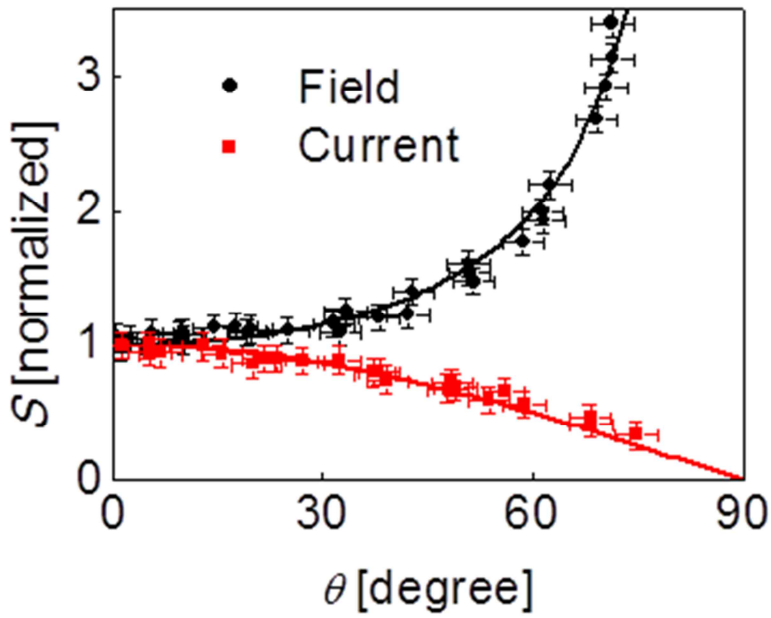

Figure 6.2 Normalized moving distance measured along fixed *h* axis with respect DW angles.

DW motion to the direction of the overall motion due to positive nonlinear coefficient. More deformation induces more positive force then the DW easily depins from the pinning site as time passes. Thus, the field driven DW roughly conserve its initial smooth shape. On the contrary to the field case, the current driven DW hardly depin from pinning site and forms facet. Figure 6.4 shows domain evolution patterns with constant current at the same position. The deformation of the DW generates a negative force due to negative λ. So, when the DW meet the strong pinning site, the DW never depins from the pinning site and entire DW morphology form facet geometry [67,68]. After the

facet formation, the speed DW is drastically reduced. Magnetization changes are depicted in figure 6.5.

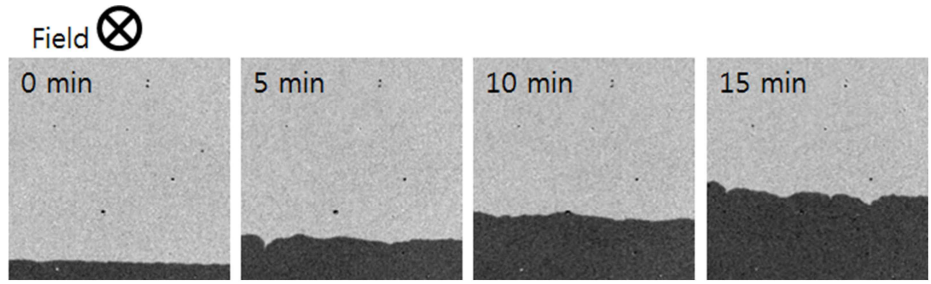

Figure 6.3 Typical DW patterns driven by a constant field (~4 Oe). Initially, a linear DW introduced in the PMA film. After the constant field applied, DW propagates upper direction. Field driven DW move with constant speed with smooth DW shape. Image size is 375 μm × 375 μm.

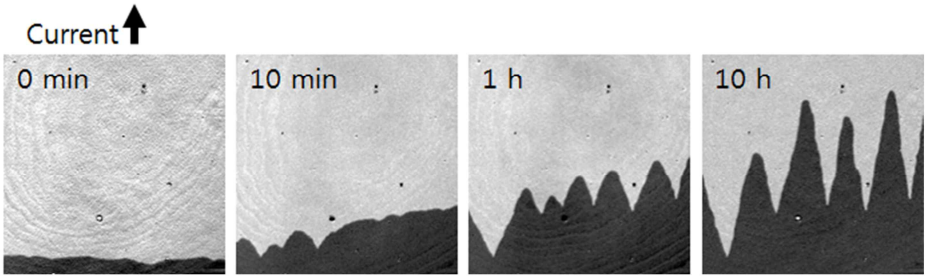

Figure 6.4 Typical DW patterns driven by a constant current (~1.2×10^{10} A/m^2). Initially, a linear DW introduced in the PMA film. After the constant current applied, the DW propagates upper direction. Current driven DW pined by strong pinning site and forms facet-like geometry. After facet formation, DW speed drastically reduced. Image size is 375 μm × 375 μm.

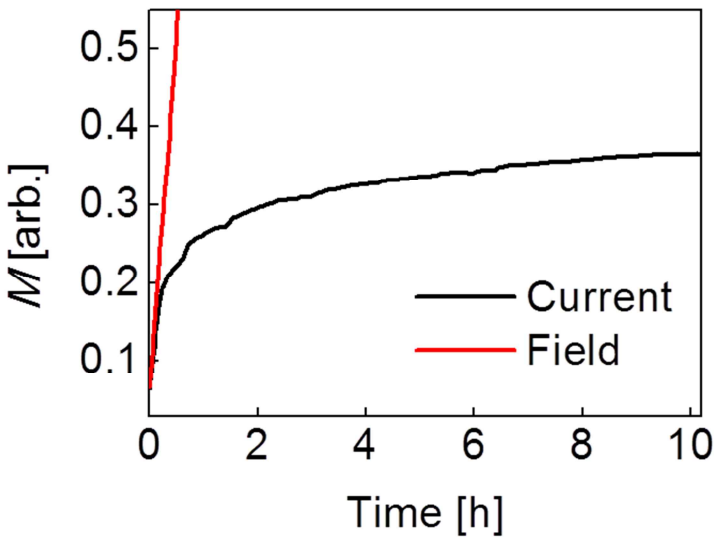

Figure 6.5 Magnetization changes induced by field and current.

6.2 DW Pattern transition

When two driving forces push same interface at the same time with opposite direction, the interface can be stopped. From equation (5.3), we extract the DW stop condition. If the current and the field drive the DW in opposite direction, the stop condition is shown as below.

$$H = -\not{d}\ \cos\theta \tag{6.2}$$

Figure 6.6 shows stabilized facets for various magnetic field with fixed positive current density (1.7×10^{10} A/m^2). Applied field oppose the driving force induced by current. When the field is zero, the facet has very sharp geometry. The angle of facet is almost 90° which

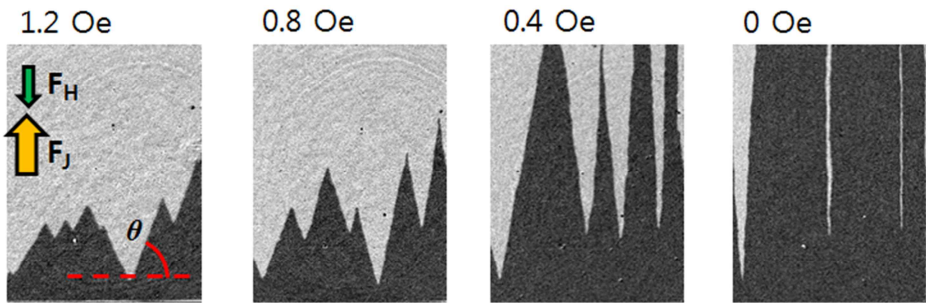

Figure 6.6 Stabilized pattern of DW with different bias field. Image size is 375 μm × 500 μm.

is expected from equation (6.2). Increasing the applied field strength, the facet angle decreases. Formed facet geometries are stable in time and DW stop. We plot facet angle with respect to applied fields in figure 6.7 and also plot equation (6.2) then we can confirm that two results are well meet to each other. So, we find out new way for determining the STT efficiency [62,69-71].

Next, we observe the DW motions when magnetic field assists the current for the DW motions. In this case, there are no stable facet DW and the DW never stop. The DW continuously inflates due to the assisting magnetic field. Figure 6.8 shows typical magnetization state

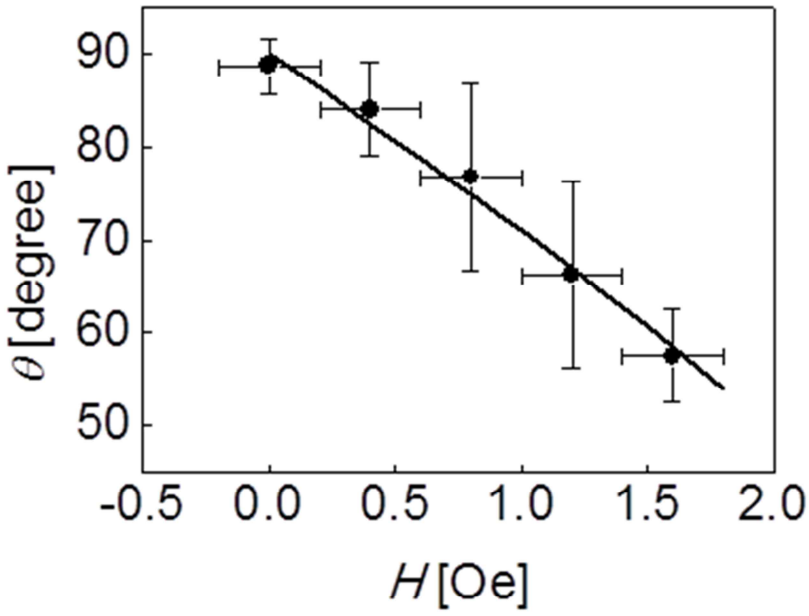

Figure 6.7 Facet angle with respect to applied field strength. Black line is obtained from equation (6.2).

change. The DW pinned by strong pinning site but depinning easily occur. The magnetization reversal induced by the DW motion occur through the entire of the film only small unreversed region left due to the dipolar field.

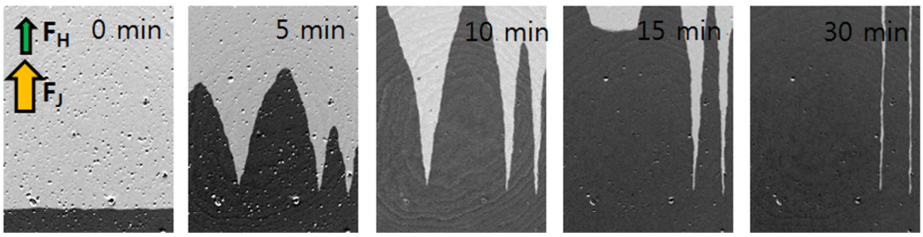

Figure 6.8 Typical pattern of DW when the field assists DW motion driven by current. Unstable facet formed and DW never stops. Image size is 375 μm × 500 μm.

6.3 Universality class of DW motion driven by field and current

Different DW morphologies represent that the DW motions driven by the field and the current belong to different universality class, respectively. However, according to the speed observation in **Chapter 5**, both the field and the current belong to the creep universality class with the creep exponent 1/4. This discordance comes from the observation range of the position and the time. Relatively short range in the position and the time, there is no influence to the DW by strong pinning site due to the probability of encounter with the strong pinning sites is sparse. Thus the DW speed obeys the generalized creep law. We measure the speed of the DW only before the facet formation. After encounter the strong pinning sites, the current driven DW speed reduce as time goes on and slowly converge to zero. So, the universality class of the DW motions depends on the range of measured space and time.

Chapter 7

Conclusion

In this thesis, we research interfaces which are driven by two distinct driving forces. For this study, we observe magnetic DWs in perpendicular magnetic anisotropy films. The research is mainly concentrated on two characters of the DW. One is the speed of the DW and the other is the shape of the DW.

Firstly, the speed of the DW driven by the magnetic field is well known as creep scaling law. In addition to this field creep scaling law, we find out that the current driven DW also belongs to creep universality class. Then we establish generalized creep equation for arbitrary angled DW.

Secondly, we observe shape of DWs driven by the field and the current. The DW shape in the field driven case forms smooth DW but current case generates facet like DW. This drastic difference comes from opposite nonlinearity which denotes angle-speed dependence. The field driven DW has positive nonlinearity but negative for current driven DW. Different shapes mean that the field and the current are belongs to different universality classes, respectively. It is quite

peculiar because speed observation represent same universality class.

This contradiction represents that universality class depend on observation range of space and time. In relatively short range, the DW motions belong to the creep universality class regardless driving forces. However, in relatively long range for the DW encounter strong pinning sites, the universality class of the DW motion are separated in creep for the field driven case, stop for the current driven case. From this result, we can expect that density distribution of pinning sites is important parameter to determine universality class. Thus, it is valuable to study disorder density distribution in PMA film.

To conclude this research, we wonder what the fundamental difference of field and current is. We think that the answer is directionality of the driving forces. The field pushes the DWs always in normal direction of DW itself, because the maximum energy gradient generated by Zeeman energy exists along perpendicular direction of DW. So, it is natural that field has no directionality or normal directionality to move the DW in the PMA films. However, the current has obvious directionality because current is a flow. Thus, directionality is a fundamental property which classifies driving forces.

Appendix

Creep criticality

Let's assume that there exist random pinning sites in 2 dimensional film structures and the DW move through the pinning sites.

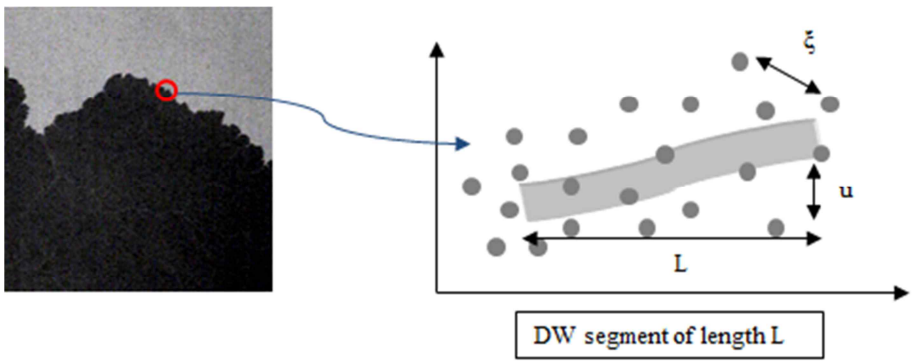

Here, the DW segment is L and the small displacement is u. Then the total free energy of the segment is as follows.

$$F(u,L) = \frac{1}{2}\epsilon_{el}\frac{u^2}{L} - \left(\Delta\xi^2 L\right)^{\frac{1}{2}} - M_s H t L u$$

Let's find the origin of the each term.

First term: tension energy (DW energy)

The DW energy is proportional to the DW length. If we obtain the length of the DW segment,

$$\text{length}: \int_0^L \sqrt{\left\{1+\left(\frac{dy}{dx}\right)^2\right\}}\,dx = \int_0^L \left\{1+\frac{1}{2}\left(\frac{dy}{dx}\right)^2\right\}dx \quad \text{where}\ \frac{dy}{dx} \sim 0$$

$$\approx L + \frac{1}{2}\left(\frac{u}{L}\right)^2 L = L + \frac{1}{2}\frac{u^2}{L}$$

Then,

$$\Delta E_1 = E_f - E_i = \frac{1}{2}\varepsilon_{el}\frac{u^2}{L} \quad \text{where,} \quad \varepsilon_{el} = 4t\sqrt{AK}(\text{DW energy per unit length})$$

Second term: pinning energy

Consider a finite-sized harmonic potential well (ξ: the characteristic length of the disorder potential)

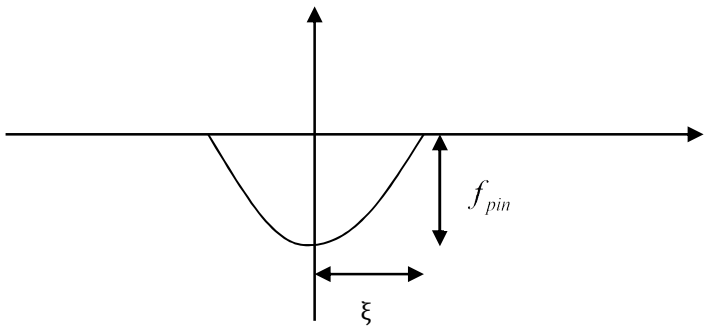

f_{pin} is the pinning force from the pinning site. The pinning site can either push or pull the DW depend on the pinning origin (magnetic inclusions or non-magnetic inclusions). The origin of the pinning site might be the extrinsic defect or intrinsic defect such as anisotropy variation.

The number of pinning sites affecting DW ~ $L \times \xi \times n_i$ (Where n_i is the surface density of pinning sites)

Pinning energy of each pinning site ~ $f_{pin} \times \xi$

$$\text{Total pinning energy : } \begin{aligned} & f_{pin} \times \xi \times \sqrt{L \times \xi \times n_i} \\ &= \sqrt{f_{pin}^2 \cdot \xi \cdot n_i} \times \sqrt{\xi^2 L} \\ &= \left(\Delta \xi^2 L\right)^{1/2} \end{aligned} \quad \text{where} \quad \Delta = f_{pin}^2 \cdot \xi \cdot n_i$$

Third term: Zeeman energy

One can easily obtain the total Zeeman energy which is proportional to the volume of magnetic system.

Definition of L_C

$$E_{el}(L_C, u=\xi) \approx E_{pin}(L_C)$$

$$\varepsilon_{el}\frac{\xi^2}{L_C} = \left(\Delta\xi^2 L_C\right)^{1/2}$$

$$\frac{\varepsilon_{el}\xi}{\sqrt{\Delta}} = L_C^{3/2}$$

$$L_C = \left(\frac{\varepsilon_{el}{}^2\xi^2}{\Delta}\right)^{1/3}$$

$$if \;\; n_i = \frac{1}{\xi^2},$$

$$L_C = \left(\frac{\varepsilon_{el}{}^2\xi^2}{f_{pin}{}^2/\xi}\right)^{1/3} = \xi\left(\frac{\varepsilon_{el}{}^2}{f_{pin}{}^2}\right)^{1/3}$$

Definition of H_{crit}

$$\varepsilon_{el}\frac{\xi^2}{L_C} = M_S H_{crit} t L_C \xi$$

$$\therefore H_{crit} = \frac{\varepsilon_{el}\xi}{M_S t}\frac{1}{L_C^2}$$

To obtain the creep criticality, we first obtain the maximum energy barrier of the system and then obtain the velocity based on the Arrhenius law.

Obtain the maximum energy barrier

Recall the total energy follows.

$$F(u,L) = \varepsilon_{el}\frac{u^2}{L} - M_S HtLu$$

There are two variables of u and L which are explained by roughness exponent as,

$$\left\langle\left\langle\left[u(x+L)-u(x)\right]^2\right\rangle\right\rangle \propto u_C^2\left(\frac{L}{L_C}\right)^{2\zeta}, for(L > L_C)$$

Here, $u_C \sim \xi$

In our magnetic films, the roughness exponent is 2/3

If we assume $x = 0,\ u(0) = 0$ then $u(L) \propto u_C\left(\frac{L}{L_C}\right)^{\zeta}$

The final total energy is as follows,

$$F(L) = \varepsilon_{el}\frac{1}{L}u_C^2\left(\frac{L}{L_C}\right)^{2\zeta} - M_S HtLu_C\left(\frac{L}{L_C}\right)^{\zeta}$$

$$= \varepsilon_{el}\frac{u_C^2}{L_C}\left(\frac{L}{L_C}\right)^{2\zeta-1} - M_S HtL_C u_C\left(\frac{L}{L_C}\right)^{\zeta+1}$$

Here the U_C and H_{crit} are defined as follows.

$$U_C = \varepsilon_{el}\frac{u_C^2}{L_C}$$

$$H_{crit} = \frac{\varepsilon_{el}u_C}{M_S t}\frac{1}{L_C^2}$$

So we can obtain the relation as $\frac{U_C}{M_S tL_C u_C} = H_{crit}$

The final total energy is

$$F(L) = \varepsilon_{el} \frac{u_C^2}{L_C} \left(\frac{L}{L_C} \right)^{2\zeta - 1} - M_S H t L_C u_C \left(\frac{L}{L_C} \right)^{\zeta + 1}$$

$$= U_C \left(\frac{L}{L_C} \right)^{2\zeta - 1} - U_C \frac{H}{H_{crit}} \left(\frac{L}{L_C} \right)^{\zeta + 1}$$

$$= U_C \left(\frac{L}{L_C} \right)^{2\zeta - 1} \left\{ 1 - \frac{H}{H_{crit}} \left(\frac{L}{L_C} \right)^{2 - \zeta} \right\}$$

To obtain the energy barrier of the system, we have to differentiate the total energy.

$$\frac{\partial F(L_M)}{\partial L} = 0$$

$$\frac{(2\zeta - 1) U_C}{L_C} \left(\frac{L_M}{L_C} \right)^{2\zeta - 2} - \frac{(\zeta + 1) U_C}{L_C} \frac{H}{H_{crit}} \left(\frac{L_M}{L_C} \right)^{\zeta} = 0$$

$$\left(\frac{L_M}{L_C} \right)^{2 - \zeta} = \frac{2\zeta - 1}{\zeta + 1} \frac{H_{crit}}{H}$$

The maximum energy barrier is determined at the length L_M

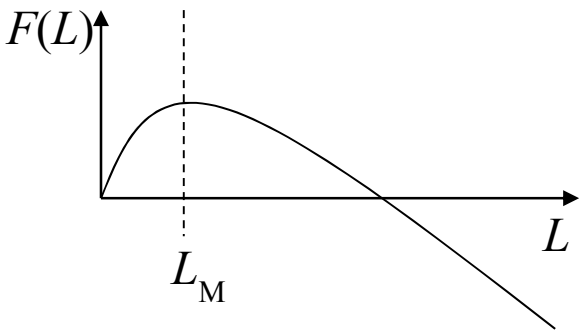

$$E_b = F(L_M) - F(0) = \frac{2 - \zeta}{\zeta + 1} \left(\frac{2\zeta - 1}{\zeta + 1} \right)^{\frac{2\zeta - 1}{2 - \zeta}} U_C \left(\frac{H_{crit}}{H} \right)^{\frac{2\zeta - 1}{2 - \zeta}} = U_C^{eff} \left(\frac{H_{crit}}{H} \right)^{\mu}$$

Where, $\mu = \dfrac{2\zeta - 1}{2 - \zeta}$

The final velocity of the DW is,

$$v(H) \propto \exp\left[-\frac{E_b}{k_B T} \right] = \exp\left[-\frac{U_C^{eff}}{k_B T} \left(\frac{H_{crit}}{H} \right)^{\mu} \right].$$

References

[1] A. Hubert and R schafer, "Magnetic domains: The analysis of magnetic microstructures." Springer, 2001.

[2] Robert C. O'Handley, "Mordern Magnetic Materials." John wiley & Sons, Inc., 2000.

[3] P. Chauve, *et al*., "Creep and depinning in disordered media." *Phys. Rev. B* **62**, 6241 (2000).

[4] S. Lemerle, *et al*., "Domain wall creep in an Ising ultrathin magnetic film." *Phys. Rev. Lett*. **80**, 849 (1998).

[5] V. Repain, *et al*., "Creep motion of a magnetic wall: Avalanche size divergence." *Europhys. Lett.* **68**, 460 (2004).

[6] F. Cayssol, *et al*., "Domain wall creep in magnetic wires." *Phys. Rev. Lett*. **92**, 107202 (2004).

[7] P. J. Metaxas, *et al*., "Creep and flow regimes of magnetic domain-wall motion in ultrathin Pt/Co/Pt films with perpendicular anisotropy." *Phys. Rev. Lett.* **99**, 217208 (2007).

[8] Kab-Jin Kim, *et al*., "Interdimensional universality of dynamic interfaces." *Nature* **458**, 740 (2009).

[9] J. C. Slonczewski, "Current-driven excitation of magnetic multilayers." *J. Magn. Magn. Mater*. **159**, L1 (1996).

[10] L. Berger, "Exchang interaction between ferromagnetic domain-wall and electric-current in very thin metallic-films." *J. Appl.*

Phys. **55**, 1954 (1984).

[11] Z. Li and S. Zhang, "Domain-wall dynamics driven by adiabatic spin-transfer torques." *Phys. Rev. B*. **70**, 024417 (2004).

[12] G. Tatara, and H. Kohno, "Theory of current-driven domain wall propagation: spin transfer versus momentum transfer." *Phys. Rev. Lett*. **92**, 086601 (2004).

[13] S. S. P. Parkin, *et al*., "Magnetic domain-wall racetrack memory.", *Science* **320**, 190-194 (2008).

[14] D. A. Allwood, *et al*., "Magnetic domain-wall logic.", *Science*, **309**, 1688-1692 (2005).

[15] S.S.P. Parkin, "Shiftable magnetic shift register and method using the same." US patent 6,834,005B1 (2004).

[16] Kab-Jin Kim, *et al*., "Electric control of multiple domain walls in Pt/Co/Pt nanotrack with perpendicular magnetic anisotropy." *Appl. Phys. Express* **3**, 083001 (2001).

[17] Y. Jaccard, *et al*., "Uniform magnetization rotation in single ferromagnetic nanowires." *Phys. Rev. B* **62**, 1141 (2000).

[18] Th. G. S. M. Rijks, *et al*., "In-plane and out-of-plane anisotropic magnetoresistance in $Ni_{80}Fe_{20}$ thin films." *Phys. Rev. B* **56**, 362 (1997).

[19] A. B. Oliveira, *et al*., "Magnetization reversal in permalloy ferromagnetic nanowires investigated with magnetoresistance

measurements." *Phys. Rev. B* **78**, 024423 (2008).

[20] J-E. Wegrowe, *et al*., "Magnetoresistance of Ferromagnetic Nanowires." *Phys. Rev. Lett.* **82**, 3681 (1999).

[21] K.-W. Moon, *et al*., "Determination of Perpendicular Magnetic Anisotropy in Ultrathin Ferromagnetic Films by Extraordinary Hall Voltage Measurement." *Rev. Sci. Instrum*. **80**, 113904 (2009).

[22] T. Ono, *et al*., "Magnetization reversal in submicron magnetic wire studied by using giant magnetoresistance effect." *Appl. Phys. Lett*. **72**, 1116 (1998).

[23] S. Tehrani, *et al*., "High density submicron magnetoresistive random access memory." *J. Appl. Phys*. **85**, 5822 (1999).

[24] S.N. Piramanayagam and K. Srinivasan, "Recording media research for future hard disk drives." *J. Magn. Magn. Mater*. **321**, 485 (2009).

[25] R. Wood, "Future hard disk drive systems." *J. Magn. Magn. Mater*. **321**, 555 (2009).

[26] S. Mangin, *et al*., "Current-induced magnetization reversal in nanopillars with perpendicular anisotropy." *Nature Materials* **5**, 210 (2006).

[27] T.A. Moore, *et al*., "High domain wall velocities induced by current in ultrathin Pt/Co/AlOx wires with perpendicular

magnetic anisotropy." *Appl. Phys. Lett*. **93**, 262504 (2008).

[28] U. Gradmann, "Magnetic surface anisotropies." *J. Magn. Magn. Mater.* **54**, 733 (1986).

[29] B. Heinrish, "Magnetic anisotropies in single and multilayered structures." *J. Appl. Phys*. **70**, 5769 (1991).

[30] S.-B. Choe and S.-C. Shin, "Magnetic field dependence of spin reversal behavior in Co/Pd nanomultilayers." *J. Appl. Phys*. **87**, 5076 (2000).

[31] J. Pommier, *et al*., "Magnetization reversal in ultrathin ferromagnetic films with perpendicular anistropy: Domain observations." *Phys. Rev. Lett*. **65**, 2054 (1990).

[32] R. D. Kirby, *et al*., "Magnetization reversal in nanoscale magnetic films with perpendicular anisotropy." *Phys. Rev. B* **49**, 10810 (1994).

[33] S.-B. Choe and S.-C. Shin, "Phase diagram of three contrasting magnetization reversal phases in uniaxial ferromagnetic thin films." *Appl. Phys. Lett*. **80**, 1791 (2002).

[34] Jeffrey R. Lindemuth and Brad C. Dodrill, "Anomalous Hall effect magnetometry studies of magnetization processes of thin films." *J. Magn. Magn. Mater*. **272**, 2324 (2004).

[35] S. Chikazumi, "Physics of Magnetism." John Wiley & Sons, Inc., 1964.

[36] J. Hur and S.-C. Shin, “New measurement techniques to determine magnetization and coercivity using a torque magnetometer.” *Appl. Phys. Lett*. **62**, 2140 (1993).

[37] L. J. van der Pauw, “A method of measuring specific resistivity and Hall effect of discs of arbitrary shape.” *Philips Res. Rep*. **13**, 1 (1958).

[38] J. Moritz, B. Rodmacq, *et al*., “Extraordinary Hall effect in thin magnetic films and its potential for sensors, memories and magnetic logic applications.” *J. Phys. D: Appl. Phys*. **41**, 135001 (2008).

[39] K.-S. Lee, *et al*., “Roughness Exponent of Domain Interface in CoFe/Pt Multilayer Films.” *IEEE Trans. Magn*. **45**, 2548 (2009).

[40] L. Thomas, *et al*., “Oscillatory dependence of current-driven magnetic domain wall motion on current pulse length.” *Nature* **443**, 197 (2006).

[41] S.-W. Jung, *et al*., “Current-induced domain wall motion in a nanowire with perpendicular magnetic anisotropy.” *Appl. Phys. Lett.* **92**, 202508 (2008).

[42] A. Thiaville, *et al.,* “Micromagnetic understanding of current-driven domain wall motion in patterned nanowires.” *Europhys. Lett*. **69**, 990(2005).

[43] R. Moriya, *et al*., “Probing vortex-core dynamics using current-

induced resonant excitation of a trapped domain wall." *Nat. Phys*. **4**, 368(2008).

[44] E. Saitoh, *et al*., "Current-induced resonance and mass determination of a single magnetic domain wall." *Nature* **432**, 203 (2004).

[45] D.-H. Kim, *et al*., "Direct Observation of Barkhausen Avalanche in Co Thin Films." *Phys. Rev. Lett*. **90**, 087203 (2003).

[46] K.-S. Ryu, *et al*., "Tunable scaling behaviour observed in Barkhausen criticality of a ferromagnetic film." *Nat. Phys*. **3**, 547 (2007).

[47] K.-J. Kim and S.-B. Choe, "Analytic theory of wall configuration and depinning mechanism in magnetic nanostructure with perpendicular magnetic anisotropy." *J. Magn. Magn. Mater*. **321**, 2197 (2009).

[48] D. Ravelosona, *et al*., "Nanometer Scale Observation of High Efficiency Thermally Assisted Current-Driven Domain Wall Depinning." *Phys. Rev. Lett*. **95**, 117203 (2005).

[49] T. Ono, *et al*., "Propagation of a Magnetic Domain Wall in a Submicrometer Magnetic Wire." *Science* **284**, 468 (1999).

[50] P. J. Metaxas, *et al*., "Magnetic domain wall creep in the presence of an effective interlayer coupling field." *J. Magn.*

Magn. Mater. **320**, 2571 (2008).

[51] The Taylor expansion is applied for cos−1(x) near x~0, where the term inside the integral is close to maximum. Up to third order expansion terms are considered. The error from this expansion is numerically verified to be less than 2% in comparison with the original equation, for our typical experimental situation.

[52] S. Honda, *et al*., "Magnetostatic energy and magnetization process in multilayers with perpendicular anisotropy." *J. Magn. Magn. Mater.* **11**, 273 (1992).

[53] J. Valentin, *et al*., "Micromagnetic analysis of magnetization reversal in CoPt alloy films." *J. Phys. D* **29**, 1111 (1996).

[54] Jan Vogel, *et al*., "Nucleation of magnetisation reversal, from nanoparticles to bulk materials." *C. R. Physique* **7**, 977 (2006).

[55] V. Repain, *et al*., "Creep motion of a magnetic wall: Avalanche size divergence." *Europhys. Lett.* **68**, 460 (2004).

[56] W. FL Bennett, *et al*., "Magnetic properties of Pd/Co multilayers." *J. Appl. Phys*. **69**, 15 (1991).

[57] J. R. Barnes, *et al*., "Magnetic force microscopy of Co-Pd multilayers with perpendicular anisotropy." *J. Appl Phys.* **76**, 2974 (1994).

[58] M. Kisielewski, *et al*., "Drastic changes of the domain size in an

ultrathin magnetic film." *J. Appl Phys.* **93**, 6966 (2003).

[59] M. Cormier, *et al*., "Effect of electrical current pulses on domain walls in Pt/Co/Pt nanotracks with out-of-plane anisotropy: Spin transfer torque versus Joule heating." *Phys. Rev. B* **81**, 024407 (2010).

[60] J. Curiale, *et al*., "Track heating study for current-induced domain wall motion experiments." *Appl. Phys. Lett.* **97**, 243505 (2010).

[61] Kab-Jin Kim, *et al*., "Joule heating in ferromagnetic nanowires: Prediction and observation." *Appl. Phys. Lett*. **92**, 192509 (2008).

[62] Jae-Chul Lee, *et al*., "Universality Classes of magnetic domain wall motion." *Phys. Rev. Lett*. **107**, 067201 (2011).

[63] Jisu Ryu, *et al*., "Magnetic domain-wall motion in a nanowire: Depinning and creep." *Phys. Rev. B* **84**, 075469 (2011).

[64] Yeon-Mu Choi, *et al*., "Self-organized interface growth with the negative nonlinearity in a random medium." *Phys. Rev. E* **66**, 047102 (2002).

[65] K.-I. Goh, *et al*., "Depinning of an anisotropic interface in random media: The tilt effect." *Phys. Rev. E* **62**, 2955 (2000).

[66] Mehran Kardar, *et al*., "Dynamic Scaling of Growing Interfaces." *Phys. Rev. Lett.* **56**, 889 (1986).

[67] Kim Sneppen, “Self-Organized Pinning and Interface Growth in a Random Medium.” *Phys. Rev. Lett.* **69**, 3539 (1992).

[68] H. Jeong, *et al*., “Facet formation in the negative quenched Kardar-Parisi-Zhang equation.” *Phys. Rev. E* **59**, 1570 (1999).

[69] T. A. Moore, *et al*., “High domain wall velocites induced by current in ultrathin Pt/Co/AlOx wires with perpendicular magnetic anisotropy.” *Appl. Phys. Lett*. **93**, 262504 (2008).

[70] Chun-Yeol You, “Critical current density for spin transfer torque switching with composite free layer structure.” *Curr. Appl. Phys*. **10**, 952 (2010).

[71] I. M. Miron, *et al*., “Domain Wall Spin Torquemeter.” *Phys. Rev. Lett.* **102**, 137202 (2009).

Author's Biography

Moon, Kyoung-Woong

THz magnetic nanodevice Lab., 23-410, Department of Physics and Astronomy, Seoul National Univ., Gwanakro, Shillim-dong, Gwanak-gu, Seoul, 151-747, Korea

Phone: +82-2-884-9254 Fax: +82-2-884-9254

E-mail: yell99@snu.ac.kr

Education

Ph.D.† Seoul National University Mar. 2006~ Aug. 2012 Physics

B.S. Seoul National University Mar. 1999~Feb. 2006 Physics

† Advisor Choe, Sug-Bong (Condensed matter physics)

Publications

1. **Kyoung-Woong Moon**, Jae-Chul Lee, Myung-Hwa Jung, Kyung-Ho Shin, Sug-Bong Choe, "Incoherent Domain Configuration Along Wire Width in Permalloy Nanowires" *IEEE TRANS. MAG*. **45(6)** 2485 (2009).

2. **Kyoung-Woong Moon**, Jae-Chul Lee, Sug-Bong Choe, Kyung-Ho Shin, "Experimental determination technique for magnetic anisotropy of individual nanowires" *CURRENT APPLIED PHYSICS* **9(6)** 1293 (2009).

3. Sung-Min Ahn, **Kyoung-Woong Moon**, Dong-Hyun Kim, Sug-Bong Choe, "Detection of the static and kinetic pinning of domain walls in ferromagnetic nanowires" *APPL. PHYS. LETT*. **95(15)** 152506 (2009).

4. **Kyoung-Woong Moon**, Jae-Chul Lee, Sug-Bong Choe, Kyung-Ho Shin, "Determination of perpendicular magnetic anisotropy in ultrathin ferromagnetic films by extraordinary Hall voltage measurement " *REV. SCI. INST*. **80(11)** 113904 (2009).

5. Lee, Jae-Chul Lee, Kang-Soo Lee, Cheong-Gu Cho, **Kyoung-Woong Moon**, Kyung-Ho Shin, Sug-Bong Choe, "Domain Patterns

and Magnetization Reversal Behaviors in Oxide/Co/Pt Films" *IEEE TRANS. MAG*. **46(6)** 2009 (2010).

6. Jae-Chul Lee, Kab-Jin Kim, Jisu Ryu, **Kyoung-Woong Moon**, Sang-Jun Yun, Gi-Hong Gim, Kang-Soo Lee, Kyung-Ho Shin, Hyun-Woo Lee, Sug-Bong Choe, "Universality Classes of Magnetic Domain Wall Motion" *PHYS. REV. LETT*. **107(6)** 067201 (2011).

7. Sung-Min Ahn, **Kyoung-Woong Moon**, Cheong-Gu Cho, Sug-Bong Choe, "Control of domain wall pinning in ferromagnetic nanowires by magnetic stray fields" *NANOTECHNOLOGY* **22(8)** 085201 (2011).

8. **Kyoung-Woong Moon**, Jae-Chul Lee, Soong-Geun Je, Kang-Soo Lee, Kyung-Ho Shin, Sug-Bong Choe, "Long-Range Domain Wall Tension in Pt/Co/Pt Films with Perpendicular Magnetic Anisotropy" *APPL. PHYS. EXPRESS* 4(4) 043004 (2011).

9. Kab-Jin Kim*, **Kyoung-Woong Moon***, Kang-Soo Lee, Sug-Bong Choe, "Control of magnetic domain-wall polarization by means of angled Oersted field writing" *NANOTECHNOLOGY* **22(2)** 025702 (2011).

10. Sung-Min Ahn, **Kyoung-Woong Moon**, Sug-Bong Choe, "Oscillatory Reduction of Domain Wall Depinning Field by Transverse Magnetic Field in Ferromagnetic Permalloy Nanowires" *JOURNAL OF NANOSCIENCE AND NANOTECHNOLOGY* **11(7)** 6472 (2011).

11.Sung-Min Ahn, **Kyoung-Woong Moon**, Cheong-Gu Cho, Sug-Bong Choe, "Control of Domain-Wall Injection Field with Different Nucleation Pad Geometry" *JOURNAL OF NANOSCIENCE AND NANOTECHNOLOGY* **11(7)** 6476 (2011).

12. **Kyoung-Woong Moon**, Jae-Chul Lee, Kungwon Rhie, Kyung-Ho Shin, Sug-Bong Choe, "Detection of Local Oersted Field Generated at the Junction Between Ferromagnetic Nanowire and Electrode" *IEEE TRANS. MAG.* **47(10)** 2508 (2011).

Presentations

1. **문경웅**, 조영진, 김광석, 이장원, 서순애, 최석봉, “L자 모양 NiFe 나노선의 자기저항 측정.” Annual Meeting of Korean Physical Society, (Oct. 2007; Korea).—*poster*

2. **K.-W. Moon**, Y. J. Cho, K. S. Kim, S. Seo, C. W. Lee, and S.-B. Choe, “Magnetoresistance Measurement of L shape Permalloy nanowires.” Annual Meeting of Korean Magnetic Society, (Dec. 2007; Korea).—*poster*

3. **문경웅**, 이재철, 최석봉, “NiFe 나노선의 회전하는 필드에 대한 자화역전 현상.” Annual Meeting of Korean Physical Society, (Apr. 2008; Korea). —*poster*

4. **문경웅**, 이재철, 최석봉, 신경호, “자기장의 방향과 NiFe 나노선의 각도에 의존하는 자화역전 현상.” Annual Meeting of Korean Magnetic Society, (Jun. 2008; Korea). —*poster*

5. **문경웅**, 이재철, 신경호, 최석봉, “NiFe 자성나노선의 폭방향으로 균일하지 않은 자화상태의 측정.” Annual Meeting of Korean

Physical Society, (Oct. 2008; Korea). —*poster*

6. **Kyoung-Woong Moon**, Jae-Chul Lee, Kyung-Ho Shin, and Sug Bong Choe, “Incoherent domain configuration along wire width in Permalloy nanowires.” Asian Magnetic Conference, (Dec. 2008; Korea). —*oral*

7. **Kyoung-Woong Moon**, Jae-Chul Lee, Kungwon Rhie, Kyung-Ho Shin, and Sug-Bong Choe, “Detection of Local Magnetic Field Generated at the Junction between Ferromagnetic Nanowire and Electrode.” Intermag, (May 2009; America). —*poster*

8. 문경웅, 이재철, 최석봉, 신경호, “펌얼로이 나노선의 자기이방상수측정.” Annual Meeting of Korean Magnetic Society, (Jun. 2009; Korea). —*poster*

9. **Kyoung-Woong Moon**, Jae-Chul Lee, Kyung-Ho Shin, and Sug-Bong Choe, “Local Magnetic Field Generated at the Junction between Ferromagnetic Nanowire and Electrode.” Annual Meeting of Korean Magnetic Society, (Dec. 2009; Korea). —*poster*

10. 문경웅, 김갑진, 이강수, 최석봉, “에르스텟 자기장을 이용

한 극성이 결정된 자구벽 쓰기.” Annual Meeting of Korean Magnetic Society, (Jun. 2010; Korea). —*poster*

11. **K. Moon**, S. Ahn, and S. Choe, “Stray-field induced domain wall pinning in ferromagnetic nanowire.” Annual Conference on Magnetism & Magnetic Materials, (Oct. 2010; America). —*poster*

12. **Kyoung-Woong Moon**, Sung-Min Ahn, and Sug-Bong Choe, “Domain Wall Pinning in Ferromagnetic Nanowire by Magnetic Nanobar.” International Conference of AUMS, (Dec. 2010; Korea). —*poster*

13. **Kyoung-Woong Moon**, Jae-Chul Lee, Kungwon Rhie, Kyung-Ho Shin, Sug-Bong Choe, “Detection of Local Oersted Field Generated at the Junction between Ferromagnetic Nanowire and Electrode.” Intermag, (Apr. 2011; Taipei). —*poster*

14. **문경웅**, 이재철, 제숭근, 이강수, 신경호, 최석봉, “자구벽의 표면장력효과.” Annual Meeting of Korean Magnetic Society, (Jun. 2011; Korea). —*poster*

15. **문경웅**, 이재철. 이긍원, 신경호, 최석봉, “Local Oersted field

generation at the junction between ferromagnetic nanowire and electrode.” Annual Meeting of Korean Magnetic Society, (Jun. 2011; Korea). —*poster*

국문 초록

자연계에서 발생하는 현상들은 수 많은 다양성에도 불구하고 공통점에 의해 몇 가지 범주로 나누어진다. 이러한 범주를 결정하는 공통점이 존재하는 이유는 대부분의 자연현상들이 표면에서 일어나고 계면의 성질이 자연현상을 결정하기 때문이다. 계면의 성질 중 형태는 계면의 정적인 성질로 대칭성과 차원에 의해 결정된다. 다른 성질로 동적인 성질인 속력이 있다. 속력은 구동력에 의존하고 구동력에 대한 특징적인 구동력-속력 관계를 나타낸다. 이 구동력-속력 관계에 의해 자연현상의 범주가 결정된다고 알려져 있다. 따라서 구동력의 세기에 따른 많은 연구들이 진행되었다.

여기서 우리는 자연현상의 범주를 결정할 수 있는 새로운 가능성을 찾아내었다. 새로운 가능성은 바로 구동력의 종류이다. 자연에는 수많은 구동력이 존재하고 각각의 구동력은 한 개의 계면에 힘을 줄 수 있다. 그래서, 구동력의 종류에 따른 연구가 이루어져야 한다. 이러한 연구를 위해 두 개의 구동력을 가지는 한 개의 계면이 필요하다.

자구벽은 자기장과 전류라는 두 가지 구동력에 의해

이동하기 때문에 다른 구동력으로 이동하는 계면을 연구하는데 적합하다. 자기장에 의한 자구벽 이동현상은 이미 이전부터 잘 알려져 왔던 사실이다. 연구들에 따르면 자기장으로 이동하는 자구벽의 속력은 크립 (creep) 이라는 범주에 속한다. 전류에 의한 자구벽 이동현상은 최근에 밝혀진 현상이다. 자기장보다 상대적으로 발견 시기는 많이 늦고 연구시간도 짧았지만, 전류에 의한 자구벽 이동현상을 이용한 다양한 응용가능성들이 제시되면서 많은 연구가 폭발적으로 이루어졌다. 특히 나노선구조를 기반으로 하는 자구벽 메모리 소자 (DW race track memory)가 대표적이다. 전류로 이동하는 자구벽의 성질 중 전류에 의한 자구벽의 속력은 장치의 동작 속도와 직결되어 있기 때문에 속력에 대한 많은 연구가 진행되었다. 연구에 따르면 전류에 의한 자구벽의 이동 속력 역시 자기장일 때와 마찬가지로 크립의 범주에 속한다는 것이 밝혀졌다.

이러한 발견이 사실이라면 자기장과 전류로 이동하는 자구벽의 형태 역시 같은 특성을 가져야 한다. 하지만 전류로 이동하는 자구벽의 형태에 대한 연구는 전무하다. 왜나하면 자구벽을 이동시킬 정도의 전류를 시료에 흘리면 전류에 의해 발생하는 줄 열 문제가 심각하기 때문이다. 이 문제를

해결하기 위해 우리는 극도로 깨끗한 수직 자기이방성 박막을 제작하였다. 이 자성 박막에 자기장을 인가하면 깨끗한 원형자구가 형성된다. 이는 제작된 박막에 존재하는 결점의 수가 극히 적고 계면을 연구하는데 있어 적합함을 의미한다.

우리는 우선 이렇게 제작된 박막의 적층 횟수에 따른 수직 자기이방성을 탐구해 보았다. 수직자기이방성상수가 클수록 자구벽은 깨끗한 형태로 만들어진다. 측정을 위해 특이 홀 효과 (extraordinaly Hall effect) 측정장비와 회전 스테이지를 구성하였다. 측정결과 수직 자성층의 적층 횟수가 한 층일 때 가장 큰 수직 자기이방성을 나타내는 것을 확인하였다.

이렇게 최적화된 자성박막을 이용하여 자기장에 의한 자구벽 이동현상을 관찰하였다. 박막의 자화상태를 관찰하기 위해 광자기 현상 (magneto-optical Kerr effect) 현미경을 사용하였다. 원형자구의 확장과 수축을 관찰하여 자구벽의 에너지를 구하였다.

또한 전류에 의한 자화상태 변화도 관찰하였다. 원형과 선형 자구에 전류를 흘리면서 자화상태 변화를 관찰한 결과 흥미롭게도 자구벽의 속력은 전류방향에 대한 자구벽의 기울기에 크게 의존하는 것으로 밝혀졌다. 이러한 속력의 각도 의존성을 연구하여 우리는 2차원박막에 존재하는 임의의

형태를 가지는 자구벽의 속력식을 완성하였다.

마지막으로, 상대적으로 긴 시간에서 자구벽 이동을 관찰하였다. 놀랍게도 전류로 이동하는 자구벽은 시간이 지날수록 산 모양 (facet)을 형성하였다. 또한 산 모양을 형성한 자구벽의 속력은 급격하게 감소한다. 하지만 자기장으로 이동하는 자구벽은 평평한 형태와 일정한 속력을 나타낸다. 이러한 차이를 만드는 이유는 비선형성계수의 부호인 것으로 밝혀졌다.

이번 연구에 의해 두 가지 구동력에 의해 한 계면의 성질이 어떻게 결정되는지 밝혀내었고 또한 자구벽 이동을 이용한 소자들을 개발하는 데 있어 이론적인 기술적인 기반을 제공하였다.

키워드: 구동력, 자구, 자구벽, 페이셋, 크립, 스핀트랜스퍼토크, 수직자기이방성

학번: 2006-20326